

Response to referee comments on “New In Situ Aerosol Hyperspectral Optical Measurements over 300–700 nm, Part 1: Spectral Aerosol Extinction (SpEx) Instrument Field Validation during the KORUS-OC cruise” by Carolyn E. Jordan et al.

On behalf of my co-authors and myself, we thank the referees for the time and effort they made in their careful review of this work. We very much appreciate their insights and suggestions which have led to revisions that we think substantively improve this manuscript. In our responses below we use gray italics for the comments from the referees, black regular font in our responses to those comments, and black italicized font for quoted material from the revision. Where we refer to line numbers, the numbers from the submitted manuscript are used in order to be consistent with the referees' comments (with the new numbers from the revision enclosed in parentheses). Track changes in the revised manuscript also make it straightforward to find all of the revised text.

Anonymous Referee #1

This paper describes the first field measurements by the spectral aerosol extinction (SpEx) instrument. The SpEx instrument measures broadband aerosol extinction at 300 - 700 nm with 0.8 nm resolution. It was deployed on a ship cruise around the Korean peninsula during May – June 2016.

The paper presents Angstrom exponents and second-order polynomial fits to the extinction data, and determines that second-order polynomial fits are a better representation.

This paper builds on previous instrument development work described in Jordan et al 2015 AMT and Chartier and Greenslade 2012 AMT.

Major comments:

1. The manuscript would be improved by examining the underlying relationship between aerosol extinction and wavelength.

As described in the introduction, the major intrinsic properties that determine aerosol extinction are the aerosol size distribution, aerosol shape, and complex refractive index. The Angstrom exponent, A (where $\text{Extinction} = k \cdot \text{wavelength}^{-A}$) is an empirical expression to describe the wavelength-dependence of the aerosol extinction. Some combinations of size distribution, shape, and complex refractive index produce extinction values that are not well-represented by an Angstrom exponent.

This paper presents Angstrom exponents and an alternative second-order polynomial fit to the extinction data. The paper would be much stronger if the authors calculated the expected aerosol extinction from the size distribution, assumed shape, and complex refractive index (volume-weighted by composition). They could then describe the types of aerosol populations that they observed during KORUS-OC that were not well-represented well by a simple Angstrom exponent and why.

We sincerely appreciate this suggestion and share the referee's interest in conducting this type of study. Unfortunately, we do not have size distribution data measured aboard the *R/V Onnuri* that we can directly compare to the optical measurements that were made. To the extent that we use the published record from KORUS-AQ to provide the overarching regional context for our measurements, that is not the same as having measurements for direct comparison. We have more recently acquired data from a subsequent field campaign where we do have commensurate size distribution and composition data and we plan to undertake the kind of study the referee recommends with that more complete data set.

2. Add a figure with a schematic of the sampling inlet, instruments connected to the sampling inlet, and flows. This is described in the text, but it would be clearer with a schematic showing the SpEx, TAP, and nephelometer with the inlet system and respective flows.

This has been added to the supplement (Fig. S2) cited in the second sentence of Section 2.1 (line 114 (146)). Note, Fig. S1 and S2 in the following sentence are not out of order as Fig. S1 is cited in the Introduction:

"The instrument suite (Fig. S2) was deployed above the bridge strapped to the starboard rail in a custom-built box designed to keep the instruments dry yet ventilated to prevent overheating (Fig. S1)."

3. Section 2 could be better organized for readability. The current organization of the paper is:

Introduction: Includes description of KORUS-OC field campaign

Section 2.1: Further description of KORUS-OC field campaign, shared sampling inlet, and instrument operation. TAP instrument is introduced here, but not defined.

Section 2.2: Description of absorption (TAP) and scattering (nephelometer) instruments, calibrations, ship plume interferences, and wavelength corrections.

Section 2.3: Description of SpEx instrument, modifications since Jordan et al 2015, and data filtering.

One suggestion for alternative headings and organization:

Section 2.1: Overview of KORUS-OC field campaign, ship, and ship tracks

Section 2.2: Description of three sampling instruments, calibrations, and data processing

Section 2.3: Description of shared instrument inlet with schematic

We have modified the text to introduce the IN101 and TAP by name earlier. At the end of the Introduction the sentence starting at line 102 (132) now reads:

"Two commercial instruments (AirPhoton's integrating nephelometer, IN101, and Brechtel's Tricolor Absorption Photometer, TAP) were also deployed to measure in situ aerosols at three visible wavelengths providing scattering coefficients and absorption coefficients, respectively."

We then revised the first paragraph of Section 2.2 and the first sentence of the next paragraph as follows:

"The IN101 and TAP instruments provide data at a higher temporal resolution than SpEx and were deployed with two objectives: 1) to identify and flag incidents of ship exhaust ("plume") contamination of the data set, and 2) to evaluate the new spectral measurements (both from SpEx and the filters). The TAP (model 2901, Brechtel, Hayward, CA) measures absorption coefficients (σ_{abs}) at 467, 528, and 652 nm with 1 s resolution and the IN101 (AirPhoton, Baltimore, MD) measures scattering coefficients (σ_{scat}) at 450, 532, and 632 nm with ~ 10 s resolution."

To identify ship plume interceptions, an initial examination of the IN101 σ_{scat} and TAP σ_{abs} data was performed."

We think these changes resolve some of the out-of-order problems that Referee #3 also noted, while preserving balance across the 3 subsections (3 paragraphs in Section 2.1, 4 paragraphs each for Sections 2.2 and 2.3).

4. It would be simpler to present all of the measurements in nm or μm throughout the paper, rather than changing from nm to μm in Section 3.3.

In our previously published work (Jordan et al., 2015) and various presentations at meetings we have consistently used nm to refer to the wavelength range of the SpEx instrument. In general, it is more convenient to use integers rather than fractional values. The switch to μm in Section 3.3 arises from the need to use units consistent with those from the Schuster et al. (2006) publication in order to compare our results to theirs. In response to comments from Referees #2 and #3 we have revised the beginning of Section 4 to include more detail on our nomenclature and the implications of Eq. (5). This includes a better explanation on the necessity to be cognizant of the units when calculating spectral curvature coefficients. We think this is an important point to make, since the calculation of α_{ext} is wavelength independent and those who use it to extrapolate measurements from a few visible wavelengths may not be aware that using nm rather than μm for curvature calculations is problematic. For this reason, keeping both sets of units in this work is more informative.

Other comments:

Line 74: Add reference to Chartier and Greenslade 2012?

We thank the referee for catching this oversight! To give Meg Greenslade the credit she is due, rather than adding a citation at line 74 we changed the first sentence in Section 2.3 to:

"Developed from a prototype described in Chartier and Greenslade (2012) SpEx is described in detail in Jordan et al. (2015)."

Line 135: Indicate that the size cut was determined theoretically.

We have updated the figure caption (note the new number due to the addition of a new Fig. S2) in the supplement to state:

"Figure S3. *Illustration of the relationship between flow rate and size cut of the sampled aerosol particles based on theoretical calculations pertinent to the system deployed aboard the R/V Onnuri.*"

Line 175: What does NT stand for? "Nephelometer TAP"?

The sentence on line 175 (232) now reads:

"For clarity, these extinction coefficients are denoted NT (for Nephelometer + TAP) σ_{ext} in comparison to the measured SpEx σ_{ext} at those wavelengths (450, 532, and 632 nm)."

Line 242: What does "Blocking" refer to? Could this be explained?

We have added a description of the Rex Block that gives the Blocking period its name in the sentence starting at line 244 (311) and broken the original sentence into 2 parts:

"The Blocking period was then characterized by limited transport and occasional brief stagnant periods due to adjacent high and low pressure systems with the high poleward of the low (called a Rex Block). Under these conditions local sources dominated pollutants, but aerosols did not accumulate to large concentrations (Peterson et al., 2019; Jordan et al., 2020a)."

Anonymous Referee #2

General Comments: This is a well written paper about an important topic: the wavelength variation of aerosol extinction. The in situ aerosol extinction data as measured by SpEx presented in this paper are convincing and an important contribution to the literature as most if not all spectral extinction data published to date are column integrated from remote sensing measurements of the total atmospheric column (AOD). However there are a few issues in the manuscript that I think should to be expanded upon or require some clarification. I think the authors should discuss in greater detail (in the text) the departure of the sampling RH from ambient by ~25% to ~30% (SpEx sampled particles are drier). This is significant since particle scattering due to particle growth increases exponentially as RH increases. See Kotchenruther et al. (1999; JGR), figure 5 of that paper. Therefore, light scattering at ambient RH under high humidity conditions would sometimes be significantly greater than that measured by SpEx. This also has potential implications for the measurement or computation of ambient single scattering albedo. Additionally, please provide some discussion on why plotting the data in spectral fit coefficient space (a_1 , a_2 ; Figs 9 & 10) is better or more informative than utilizing the two spectral parameters of Angstrom Exponent (AE; for say 370-700 nm) and its Curvature (AE') as defined by a 2nd order fit of extinction versus wavelength (logarithmic), again over the entire

measured WL range. It would seem to be more physically intuitive to most readers to analyze the data in this manner than to analyze and plot the fit coefficients. I suggest acceptance by the journal after the above and following comments/suggestions have been considered, and the manuscript revised in response.

The point about RH is very well taken. We have revised the text to clarify our approach, specifically in response to the comment about Page 4 Line 123-124 below, which we copy here for your convenience:

We have clarified the text earlier in this paragraph (line 149 of revised manuscript) to explain that when we say measurements were at ambient, we mean that the aerosols were not dried prior to sampling. We then updated the conclusion of the paragraph as follows:

"The primary objective in this work is to evaluate the performance of SpEx by direct comparisons to the data from the two commercial instruments in the measurement suite. Hence, we did not perform any corrections to either ambient T and RH or to standard temperature and pressure (STP) prior to comparing these data. There are no comparisons in this pair of manuscripts to other data sets, so such corrections are not necessary for this study."

As for the referee's second point above, as detailed in our responses to the specific comments below, we have more fully described the wavelength dependence of the curvature coefficients in Section 4 of the revised manuscript, including a much better explanation of the importance of the characteristic wavelength (λ_{ch}) of the measurement. We now summarize that expanded discussion in the abstract (starting at line 31 of both versions of the manuscript) as follows:

"Building on previous studies that used total column AOD observations to examine the information content of spectral curvature, the relationship between α and the second order polynomial fit coefficients (a_1 and a_2) was found to depend on the wavelength range of the spectral measurement such that any given α maps into a line in (a_1, a_2) coefficient space with a slope of $-2\ln(\lambda_{ch})$, where λ_{ch} is defined as the single wavelength that characterizes the wavelength range of the measured spectrum (i.e., the "characteristic wavelength"). Since the curvature coefficient values depend on λ_{ch} , it must be taken into account when comparing values from spectra obtained from measurement techniques with different λ_{ch} . Previously published work has shown that different bimodal size distributions of aerosols can exhibit the same α , yet have differing spectral curvature with different (a_1, a_2). This implies that (a_1, a_2) contain more information about size distributions than α alone. Aerosol size distributions were not measured during KORUS-OC and the data reported here were limited to the fine fraction, but the (a_1, a_2) maps obtained from the SpEx data set are consistent with the expectation that (a_1, a_2) may contain more information than α , a result that will be explored further with future SpEx and size distribution data sets."

Specific Comments:

Page 2, Lines 35-36: Perhaps this sentence should be re-written to suggest that the combination of both Angstrom Exponent and spectral curvature information provides the most information related to particle size distribution.

We have revised this part of the abstract (starting at line 31 of both versions of the manuscript, please see our response to your overall comments above).

Page 3, Lines 65-66: I think this statement is too strong. Hyperspectral data are not really required since the wavelength dependence of extinction varies smoothly with wavelength. Therefore sufficient wavelength sampling does not need to be hyperspectral, but does require several narrowband spectral measurements spanning the UV, visible and NIR wavelengths.

We have revised the sentence on lines 65-66 (82-84) as follows:

"However, if α is not, in fact, wavelength-independent for ambient aerosols, then a hyperspectral measurement (or sufficient wavelength sampling spanning the full wavelength range of interest) is required to capture the actual wavelength dependence."

Page 3, Lines 67-74: It would be appropriate in this section to also discuss the work of O'Neill et al. (2001, 2003) that utilized the 2nd order fit to AOD spectra (parameter AE') and AE to separate fine mode versus coarse mode AOD components. This algorithm was also successfully applied by Kaku et al. (2014; AMT) to in situ air sampling instrumentation on ship to determine fine and coarse mode extinction components.

Thank you for this suggestion. The intent of that paragraph was focused on the influence of aerosol microphysical and chemical properties on spectral shape and how SpEx can relate the latter to other in situ observations of the former. However, we had not thought to also mention how it can provide a new link between in situ observations and retrievals. We have revised the end of that paragraph (starting at line 92 of the revised manuscript) as follows:

"Recently, the retrieval algorithm developed by O'Neill et al. (2001, 2003, 2008) to distinguish fine mode from coarse mode AOD components using 2nd order spectral fits has been applied to in situ extinction components based on scattering and absorption measurements made at a few visible wavelengths and evaluated using several sets of field data (Kaku et al., 2014, and references therein). The Spectral Aerosol Extinction (SpEx) instrument (Jordan et al., 2015) provides a new measurement approach that combines the advantages of a broad spectral range (typically limited to remote sensing techniques) with an in situ measurement capability (that allows for direct comparison to other in situ measurements of ambient aerosol microphysical and chemical properties). Combining this hyperspectral in situ measurement capability with retrieval techniques as in Kaku et al. (2014) also provides a new tool to fine tune remote sensing retrievals."

We then relocated the text citing the spectral resolution to the next paragraph and updated the conclusion of that paragraph to again emphasize the ability to use SpEx to relate in situ spectral extinction to aerosol microphysics and composition as follows:

"Hence, SpEx is particularly suited to examine spectral details for ambient aerosols over its measurement range and to relate those spectral details to simultaneous in situ measurements of ambient aerosol microphysics and composition."

Page 4, Lines 94: FOV is typically used to define pixel size, so perhaps viewing region or something like that is more accurate in the context of this sentence.

We have changed this to field of regard (line 123 of the revised manuscript, field of view was used by mistake, thanks for catching this!).

Page 4 Line 123-124: It would be very useful to be clearer here. Did you make adjustments to bring the SpEx data close to ambient conditions or leave them as extinction spectra of partially dried aerosol?

We have clarified the text earlier in this paragraph (line 149 of revised manuscript) to explain that when we say measurements were at ambient, we mean that the aerosols were not dried prior to sampling. We then updated the conclusion of the paragraph as follows:

"The primary objective in this work is to evaluate the performance of SpEx by direct comparisons to the data from the two commercial instruments in the measurement suite. Hence, we did not perform any corrections to either ambient T and RH or to standard temperature and pressure (STP) prior to comparing these data. There are no comparisons in this pair of manuscripts to other data sets, so such corrections are not necessary for this study."

Page 8 Line 271-272: The slope of near unity occurs in Figure 3 since it seems that both instruments have partially dried aerosol with RH lower than ambient by ~25% to ~30%. Perhaps this should be mentioned in the text when discussing this Figure.

We think that with the revised text in section 2.1 (shown in our response to your recommendation above) accomplishes this.

Page 9 line 305: Please discuss why the data are noisier in Fig 7 at the longest wavelength end of the SpEx measured extinction coefficients. Is this consistent for all measured spectra from SpEx? Is this random variation or does it depend on temperature or some other variable?

This is partly an optical illusion due to the log scale used to plot the spectra. Nonetheless, the calculation of σ_{ext} (Eq. 4) is sensitive to the difference in the sample and reference spectra such smaller reference values (I_0) combined with small differences between I and I_0 lead to greater uncertainty in σ_{ext} . We have added the following text at the end of the paragraph you reference (starting at line 392 of the revised manuscript) to explain this as follows:

"Note, the log scale used to plot the spectrum (red curves) in Fig. 7 along with the relatively small extinctions at long wavelengths exaggerates the appearance of noise at those wavelengths (i.e., $\pm 5 \text{ Mm}^{-1}$ at the red end where $\sigma_{\text{ext}} \sim 20 \text{ Mm}^{-1}$, $\text{LN}(20) \sim 3$, is more obvious than in the UV where $\sigma_{\text{ext}} \sim 150 \text{ Mm}^{-1}$, $\text{LN}(150) \sim 5$). Nonetheless, the intensity of the xenon lamp decreases from 600 to 700 nm (Fig. S4; in Fig. 7, $\text{LN}(0.6 \mu\text{m}) \sim -0.51$, $\text{LN}(0.7 \mu\text{m}) \sim -0.36$) such that smaller values of I_0 combined with the small differences between I and I_0 in this wavelength range lead to slightly greater uncertainty in σ_{ext} (Eq. (4))."

Page 11 line 353, equation 5: It would be useful to state that $-2a_2$ is equal to the parameter AE' which defines the curvature of extinction spectra, $AE' = -dAE/d \ln \lambda$.

Following Eq. (5) we have added the following sentence:

"Note, the derivative of Eq. (5), $\alpha_{ext}' = -d\alpha_{ext}/d \ln(\lambda) = -2a_2$ defines the curvature of the extinction spectra (Eck et al., 1999)."

Page 11 line 366-367: Note that another significant difference between the SpEx extinction coefficient data and AERONET AOD data is that in the total atmospheric column measured by AERONET there is always some variable amount of coarse mode particles present, while the SpEx sampling excludes all coarse mode particles and even the shoulder of some very large fine mode particles (see Dall'Osto et al., 2009 and Eck et al. 2018). Coarse mode (super-micron sized radius) particles have Angstrom Exponent close to zero (actually slightly negative) and also curvature near to zero. I suspect that this difference in particle size sampling is of greater importance than the spectral range since the 2nd order fit is excellent with AERONET data (within measurement uncertainty) throughout the 380 to 870 nm wavelength range. Note that the 1020 nm AOD data in the AERONET database in 2006 had greater uncertainty due to water vapor absorption in the Schuster et al. 2006 paper than current V3 data and also that the 340 nm channel has significantly larger uncertainty than the other measured wavelengths due to interference filter issues (out-of-band blocking & higher transmission degradation rate at this wavelength). For these reasons both the computation of AE' (Eck et al., 1999, 2001 etc) and SDA retrievals (O'Neill et al. 2001, 2003 etc) of fine and coarse AOD only utilize the 380, 440, 500, 675 and 870 nm wavelengths from the AERONET database. Also the 340 nm and 1020 nm are excluded from the AOD input to the SDA algorithm in the AERONET database due to significantly larger uncertainties and potential biases at those wavelengths.

We clearly failed to adequately explain λ_{ch} in the submitted version. Based on your comments and those of Referee #3 we have substantially rewritten Section 4. We have clarified at the start of the section (line 431 of the revised manuscript) that we only compare our results to the appropriate subset of data in Schuster et al. (2006):

"A comparison of the coefficients obtained from SpEx to the fine fraction subset of aerosols reported in Schuster et al. (2006) revealed two key differences between the data sets."

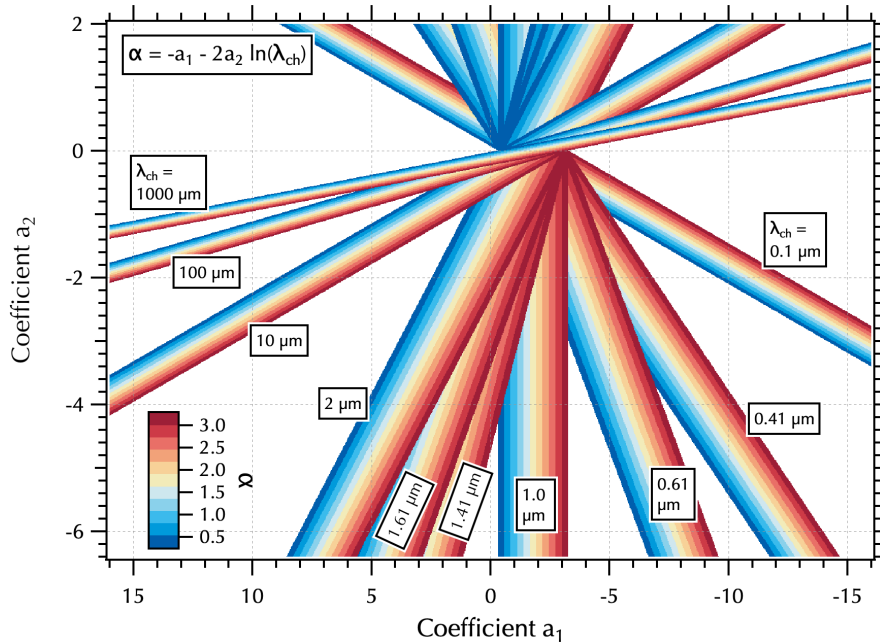
We have revised the paragraph following Eq. (5), starting at line 441 of the revised manuscript, and added two new paragraphs to better explain how differing values of λ_{ch} lead to rotation in (a_1, a_2) space (note, we include Fig. S8 below for your convenience):

"Note, the derivative of Eq. (5), $\alpha_{ext}' = -d\alpha_{ext}/d \ln(\lambda) = -2a_2$ defines the curvature of the extinction spectra (Eck et al., 1999). For any given spectrum, there is one wavelength at which the linear and 2nd order polynomial fits yield equivalent results in Eq. (5). This must not be confused with every wavelength measured in the spectrum, so we will refer to this one wavelength as the characteristic wavelength of the measurement range, λ_{ch} , from here on. It can be calculated for each measured spectrum from the two sets of fit coefficients for that spectrum. That is, rewriting Eq. (5) in terms of λ_{ch} the characteristic wavelength of the measured spectrum may be calculated

from $\lambda_{ch} = e^{((\alpha_{ext} + a_1) / -2a_2)}$. For the SpEx data set, λ_{ch} was found to range from 0.36 - 0.46 μm . In contrast, the empirical fit of $\alpha_{ext} = a_2 - a_1$ implies $\lambda_{ch} \sim 0.61$, i.e., $\ln(0.61) \sim -0.5$. The dependence of Eq. (5) on the characteristic wavelength, results in spectra sets with differing λ_{ch} exhibiting different mapping between α_{ext} and (a_1, a_2) . To illustrate this, consider the range of α_{ext} values (0.29 - 3.25) found from linear fits over 0.3 - 0.7 μm to all of the spectra measured by SpEx during KORUS-OC. This range of α_{ext} values maps differently into (a_1, a_2) space as a function of λ_{ch} (Fig. 9, top right panel).

There are two special cases evident in Eq. (5) that result in $\alpha_{ext} = a_1$. First, when there is no curvature ($a_2 = 0$), a_1 describes the same linear fit as α_{ext} . Second, when $\lambda_{ch} = 1 \mu\text{m}$ (i.e., $\ln(1) = 0$) Eq. (5) is insensitive to curvature such that a_2 can have any value at all. This can be understood from Eq. (1), where α can be any value when $\lambda = 1 \mu\text{m}$ and $p(1\mu\text{m})$ will always = β . The former leads to all λ_{ch} sets overlapping at $a_2 = 0$, while the latter exhibits a broad vertical band independent of curvature (a_2) (Fig. 9, top right panel). These special cases have important implications. As λ_{ch} approaches 1 μm the measurement becomes insensitive to curvature, while at the short wavelengths of light represented by $\lambda_{ch} < 0.1 \mu\text{m}$ the curvature itself becomes unimportant. Hence, to probe spectral curvature the upper right panel of Fig. 9 shows measurement techniques with $\lambda_{ch} \sim 0.5 \pm 0.2 \mu\text{m}$ provide the greatest sensitivity with sufficient separation in (a_1, a_2) to distinguish aerosol microphysical and chemical properties influencing the spectral shape.

The rotation as a function of λ_{ch} shown in Fig. 9 also illustrates why wavelength units of μm must be used to calculate (a_1, a_2) . As λ_{ch} increases to values $> 1 \mu\text{m}$, the α map rotates clockwise (Fig. S8). If one used $\lambda_{ch} = 410 \text{ nm}$ rather than $0.41 \mu\text{m}$, it would map into a narrow band in the next quadrant of (a_1, a_2) space spanning a wide range in a_1 but a narrow range in a_2 , resulting in little curvature sensitivity. The calculation of α_{ext} is wavelength independent and will produce the same result no matter what units are used. This is not the case for the calculation of (a_1, a_2) , so it must be emphasized that for curvature, the units matter."



"Figure S8. Illustration of the rotation of the mapping of α in (a_1, a_2) space as a function of λ_{ch} for long wavelengths. This illustration includes the extreme values of λ_{ch} of 100 and 1000 μm to stand in for the mapping that arises from using nm units instead of μm of wavelength."

We anticipate that when we have SpEx data representative of coarse (or bimodal size distributions) that the (a_1, a_2) coefficients obtained from those data sets will also be rotated from comparable size distributions in Schuster et al. (2006) due to the shorter λ_{ch} of the SpEx measurement.

Page 12 line 419-421: It seems that only full spectra (or at least encompassing the wavelength extremes and mid-point) should be analyzed. This is the strategy with making SDA retrievals from AERONET data at Level 2 (publication quality). For AERONET the 380, 500 and 870 nm wavelengths at a minimum must be available thus encompassing the minimum, maximum and middle wavelengths over the wavelength range considered. This ensures an accurate characterization of the non-linearity of the AOD spectra. The other possible wavelengths are 440 and 675 nm and are utilized in addition to the minimum three, if available.

This is an important point but bear in mind that there are different potential uses of the SpEx data. One would not want to use the partial spectra for a retrieval, but the above detection portion of the spectrum might still be used in combination with absorption measurements (as in Part 2) to look at the structure of single scattering albedo in the UV even in cases where ambient concentrations at longer wavelengths in our instrument are below detection. We have added the following text to the end of that paragraph (starting at line 583 of the revised manuscript):

"Note, partial spectra are not suitable for retrievals (i.e., comparable to those from AERONET Level 2 data where at a minimum above detection values must be available from at least the 0.38, 0.50, and 0.87 μm channels to ensure nonlinearity in the spectrum is adequately represented). However, partial spectra can be valuable for other analyses such as when

combined with absorption coefficients in the calculation of $\omega(\lambda)$ to look for structure in the above detection range for SpEx, particularly in the UV (see Part 2, Jordan et al., 2020b). Hence, partial spectra data are not discarded from further examination."

Figure 7, x-axis labeling and caption: It would be much more useful for most readers if you label the x-axis in wavelength (with logarithmic scale) either in nm or microns not as logarithm of wavelength.

The reason we use the logarithmic units on the axes of Fig. 7 is the values of the coefficients depend on those units, specifically on the natural log of wavelength in microns (as well as the natural log of σ_{ext} in Mm^{-1}). Only α is independent of the units as is now fully explained in the text (please see above response regarding revisions to Section 4). However, to aid the reader we have included the wavelength values in μm in the figure caption that correspond to the $\text{LN}(\lambda(\mu\text{m}))$ x-axis labels. We have also clarified what the linear fit coefficients in Fig. 7 (a, b) represent in terms of β and α :

"Figure 7. Example of wavelength dependence of $\text{LN}(\sigma_{\text{ext}} (\text{Mm}^{-1}))$ spectra (red curves) as a function of $\text{LN}(\text{wavelength } (\mu\text{m}))$. Linear ($y = a + b(x)$, left panels; here the intercept $a = \text{LN}(\beta)$, the value of $\text{LN}(\sigma_{\text{ext}})$ at $1 \mu\text{m}$ where $\text{LN}(1 \mu\text{m}) = 0$, and the slope $b = -\alpha$) and 2nd order polynomial ($y = a_0 + a_1(x) + a_2(x^2)$, right panels) fits (black curves) are shown with the fit residuals ($= \text{LN}(\sigma_{\text{ext}} (\text{Mm}^{-1})) - \text{fit}$, blue curves). Residuals randomly distributed around zero indicate a good fit by the mathematical function used to fit the data, trends in residuals suggest another function may provide a better fit. Top and bottom panels show fits to a subrange ($\text{LN}(0.450 - 0.632 \mu\text{m})$) and full range ($\text{LN}(0.3 - 0.7 \mu\text{m})$) of the measured spectrum, respectively. Middle panels show the extrapolation of the fit in the top panels over the full measured wavelength range. The x-axis labels of -1.2, -1.0, -0.8, -0.6 and -0.4 for $\text{LN}(\lambda (\mu\text{m}))$ equal 0.301, 0.368, 0.449, 0.549, 0.670, and 0.698 μm wavelengths, respectively."

Anonymous Referee #3

This manuscript describes spectrally resolved aerosol extinction measurements taken with a White-type optical cell during KORUS-OC campaign during the summer of 2016. The performance of the system was evaluated by comparison to the sum of scattering and absorption measurements done with commercially available instruments. Perhaps the most significant issue discussed in this manuscript is the pitfall in using the extinction Angstrom exponent (EAE) to describe the spectral dependence of optical properties. The authors compare and discuss the advantages of alternatively using a 2D parameter space (namely, the two first fitting parameters of a 2nd order polynomial fit).

I recommend this manuscript be published after addressing the following comments.

General comments:

1) The title of the manuscript does not seem to describe the main topic I understood it. From the title, it would seem that the field validation is the main topic while to me it seemed almost the trivial part. There is no mention in the title of the fact that the instrument was used to compare and discuss the advantages of an alternative to the EAE.

This is an interesting observation. We don't think changing the title is an option at this point (the editor can correct us if we are wrong about that). For us, the primary objective of this paper is to publish a methods paper that describes the instrument in detail that we can cite in future work and that demonstrates that the instrument works well. The secondary objective is to preemptively address a comment/question that the lead author has gotten every time this work has been presented that takes some form of "why is this useful when we can just calculate the spectrum using Angstrom exponents?". Part of the reason that it took so long to prepare this manuscript for publication was in trying to understand why the spectra were not linear as expected, then upon discovering the rich literature on spectral curvature from the remote sensing retrieval community, why the curvature coefficients from SpEx did not agree with those in Schuster et al. (2006). And so, the manuscript over time developed two somewhat distinct parts: validating the method with the commercial instruments and applying the Schuster et al. (2006) analytical approach to the data (both here and in Part 2). We anticipate a variety of analytical approaches one could take with the SpEx measurements, depending on the subject of inquiry. If the editor agrees that the title should be amended, we would be willing to consider alternatives.

2) I believe that the manuscript could be much better organized. The text often refer the reader to plots not in the order of their appearance and to several plots at the same line. This makes it a bit less readable and difficult to follow the story.

We checked the manuscript and the figures are introduced in order. We do make comparisons across figures, so perhaps referring back to a previously introduced figure has caused some confusion. The other concern here may be related to our choice of showing the 532 nm comparisons in the main text yet including the 450 and 632 nm comparisons in the supplement (this accounts for the times we point to Fig. 4, S6, and S7, for example). The reader does not need to refer to the figures in the supplement. The main figures are sufficient. Nonetheless, for the purpose of validating the performance of the instrument we wanted keep the other two wavelengths in the record.

3) The use of the 2D parameter space as an alternative to EAE (i.e. to derive information on the aerosol size distribution) is discussed only in the context of the data presented here. I believe it would strengthen the manuscript to add a more general discussion, perhaps with the aid of simulated data.

For this we recommend Schuster et al. (2006).

4) The reason for the large errors in fitting an EAE to spectral data, namely "larger" particles is not mentioned (aside from one sentence towards the end of the manuscript, line 417-418). The curvature aspect of the log-log data can be easily explained in terms of Mie theory for light extinction by spherical particles. The classical Qext Vs size parameter curve shows smooth increase behavior for "small" size parameters while it wiggles over "larger" size parameters

due to Mie resonances. “larger” size parameters mean larger particles and/or shorter wavelengths. It is these wiggles (due to Mie resonances) that cause the apparent deviation from power law behavior. The larger the particles (and/or shorter the wavelength) the more wiggles fit into the measured spectral window and more orders are needed for a reasonable fit using a polynomial. This means that the smaller the mode diameter and the smaller the sd of the aerosols size distribution the more likely the measured log-log spectrum will be adequately represented with a linear (1st order polynomial) fit.

Thank you for the very interesting observations. Since we have not done Mie calculations as a part of this work, we have not discussed the results in these terms. As mentioned previously both in the manuscript and in this response to Referee #1, we did not measure size distributions (SD) aboard the *R/V Onnuri*. Thus, we cannot use measured SDs to provide insight, either. We anticipate a future publication using more recent data where we have both SpEx data and size distributions to give us an opportunity to relate our observations to Mie theory calculations and present such a discussion.

5) My impression was that there is a fair amount of text and some figures that are not essential to deliver the main message. removing them (maybe to the supplementary material) would some room for more needed discussion.

Thank you. We hope that the reviewer finds a more focused document in the latest manuscript.

6) A few simple simulations that I did showed inverse (almost) linear relationship between a_2 and a_1 . This manuscript shows a positive (almost) linear relationship (note the inverted x-axis in figures 9 and 10. I could be mistaken but I suggest the authors take a second look to check this issue.

Thank you. We did check again and obtained the same result. Did you use nm or μm ? The choice in units matters here as discussed below and in greater detail in the revised text.

Specific comments:

Line 28: I suggest using the convention of EAE (Extinction Angstrom Exponent) rather than α which can be easily confused with the symbol often used to describe extinction coefficient.

Too many redundant symbols for common parameters is always a problem in our business. We have adopted a nomenclature herein to avoid confusion with the use of AE / AE'. We chose the Greek symbol α because it is commonly used to represent the extinction Angstrom Exponent in the literature.

Line 33-35: after reading the final part of the abstract several times I still don't understand what is exactly the message here. The characteristic wavelength is not a well-known property of aerosol population and is not explained in the abstract. Therefore, to me it sounds like one would need to read the whole paper to understand this part. This is surly not something you would want for the abstract. Additionally, (1) “such that . . . aerosol size distributions with the same α . . .”

how can different size distribution of aerosols have the same α ? Isn't it true that α is heavily dependent on the size distribution? (2) is the slope related to λ_{ch} or is it the λ_{ch} ?

This is a very good point. The characteristic wavelength is a term we define (for the first time, we believe) in this work. And as you will see below, we have a more extensive discussion of this in the revised text of Section 4. Here, we have updated the abstract (starting at line 31) to more fully explain both λ_{ch} and the idea behind the greater information content of (a_1, a_2) as follows:

"Building on previous studies that used total column AOD observations to examine the information content of spectral curvature, the relationship between α and the second order polynomial fit coefficients (a_1 and a_2) was found to depend on the wavelength range of the spectral measurement such that any given α maps into a line in (a_1, a_2) coefficient space with a slope of $-2\ln\lambda_{ch}$, where λ_{ch} is defined as the single wavelength that characterizes the wavelength range of the measured spectrum (i.e., the "characteristic wavelength"). Since the curvature coefficient values depend on λ_{ch} , it must be taken into account when comparing values from spectra obtained from measurement techniques with different λ_{ch} . Previously published work has shown that different bimodal size distributions of aerosols can exhibit the same α , yet have differing spectral curvature with different (a_1, a_2) . This implies that (a_1, a_2) contain more information about size distributions than α alone. Aerosol size distributions were not measured during KORUS-OC and the data reported here were limited to the fine fraction, but the (a_1, a_2) maps obtained from the SpEx data set are consistent with the expectation that (a_1, a_2) may contain more information than α , a result that will be explored further with future SpEx and size distribution data sets."

Line 81: it is not clear to me what the authors meant by "2 nm resolution in intensity"

The resolution of polarimeters is described both in terms of the spectral resolution for intensity and for the degree and angle of linear polarization. For the sake of the comparisons in this paragraph the resolution in intensity is the parameter of interest.

Line 117: TAP is not defined.

In response to Referee #1's request to improve the readability of Section 2 we now introduce the TAP (and IN101) at the end of the Introduction (starting at line 102 (132)), resolving this problem:

"Two commercial instruments (AirPhoton's integrating nephelometer, IN101, and Brechtel's Tricolor Absorption Photometer, TAP) were also deployed to measure in situ aerosols at three visible wavelengths providing scattering coefficients and absorption coefficients, respectively."

Line 135: sampling off (from/by/using?) the same inlet line?

We have rephrased this (line 135 (170)) to *"sampling from the same inlet"*.

Line 141-142: "as the ship. . . at that time". It is not clear to me what do you mean by "restarting the system". I also feel this sentence does not contribute to the manuscript.

This was intended to explain why the data set ended well short of port even before entering the Territorial Seas. However, it is a minor point that is not essential so we have removed that sentence and part of the preceding sentence. The conclusion of Section 2.1 now reads:

"They also ensured that the system ran properly and were there to handle problems. The methodology and results of the filter sampling will be presented in the companion paper (Part 2, Jordan et al., 2020b)."

Line 148-149: the internet links are not needed and in my opinion reduce readability.

As with the introduction of the term TAP, we have revised this text primarily in response to Referee #1's request to revise Section 2. We have also removed the internet links from lines 148-149 (180-182):

"The TAP (model 2901, Brechtel, Hayward, CA) measures absorption coefficients (σ_{abs}) at 467, 528, and 652 nm with 1 s resolution and the IN101 (AirPhoton, Baltimore, MD) measures scattering coefficients (σ_{scat}) at 450, 532, and 632 nm with ~10 s resolution."

Line 165: here, the reader is asked to compare figure S3 and figure 2 but there is no explanation as to what is the difference between the two figures. It should also be made clear that this data was acquired by using the TAP and IN.

We have updated the parenthetical in the sentence on line 165 (221-222) as follows (note the new number, S4, due to the addition of the new Fig. S2):

"(the interested reader can compare σ_{abs} in Fig. S4 that shows all of the data in the time series including ship plume interceptions to σ_{abs} in the top panel of Fig. 2 where the plume interceptions have been removed)"

Line 174: a discussion about the errors generated from the wavelength adjustment is needed.

It is important to remember that scattering is the dominant term in NT σ_{ext} by about an order of magnitude, so the small wavelength adjustments made to shift σ_{abs} from 467 to 450 nm, 528 to 532 nm, and 652 to 632 nm make a negligible contribution to the error of NT σ_{ext} .

Line 263-265: how were local ship emissions distinguished from emissions of the research vessel?

We have appended the following sentence to the end of that paragraph (starting at line 334 of the revised manuscript):

"Note, the inference that aerosols during the Blocking period were from local ship emissions refers to the regional ambient environment and should not be confused with ship plume contamination from the R/V Onnuri (see Section 2.2 for the criteria used to remove ship stack contamination from the data set)."

Line 272: the plot referring to the 632nm channel shows that all fitted lines consistently show 5-9% over estimation of extinction from sum of scattering and absorption compared with measured extinction. What could be the cause? How accurate are the absorption measurements in this wavelength? Is it possible that these have a positive bias?

Scattering is the dominant term here, so the contribution of absorption to the bias is likely to be small. As we discuss in Section 2.2 (lines 156-157 (212)) we were unable to perform calibrations of the nephelometer during the cruise (as is customary for this kind of measurement) and had to instead rely on pre-and post-deployment calibrations performed in our laboratory. Whether the bias you note is a fundamental characteristic of this particular IN101 or was a singular occurrence due to inadequate calibration of the nephelometer throughout the deployment is unknown. We will continue to evaluate this question with more recent data sets.

Line 280-281: it is not clear to me what is meant here by “10 s scat and 1 s abs measurement for every ext spectrum. Please explain.

We have revised the preceding sentence (lines 279-280 (351-353)) to clarify this:

"This is partly attributable to the differing noise characteristics of the measurement techniques, but it also arises from differences in sampling intervals where the standard error of the means reduces the variability by the square root of the number of samples in the mean."

Line 303: it would be beneficial to choose one unit system (wavelength in nm or μm) and be consistent throughout the manuscript.

Referee #1 made a similar comment (major comment #4). For your convenience, we copy the response to that here:

In our previously published work (Jordan et al., 2015) and various presentations at meetings we have consistently used nm to refer to the wavelength range of the SpEx instrument. In general, it is more convenient to use integers rather than fractional values. The switch to μm in Section 3.3 arises from the need to use units consistent with those from the Schuster et al. (2006) publication in order to compare our results to theirs. In response to comments from Referees #2 and #3 we have revised the beginning of Section 4 to include more detail on our nomenclature and the implications of Eq. (5). This includes a better explanation on the necessity to be cognizant of the units when calculating spectral curvature coefficients. We think this is an important point to make, since the calculation of α_{ext} is wavelength independent and those who use it to extrapolate measurements from a few visible wavelengths may not be aware that using nm rather than μm for curvature calculations is problematic. For this reason, keeping both sets of units in this work is more informative.

Line 350-355: this is an important paragraph which I strongly feel that is not explained properly. (1) “The two expressions used here to fit the relationship between σ_{ext} and λ are related by their negative derivative, defined as α in Eq. (2)”. Eq. 2 applies by definition only to the linear fit so how does it relate the linear fit to the 2nd order poly’ fit? (2) “the derivative of the linear fit ($y=a+bx$; $dy/dx = b$) equals the derivative of the 2nd order polynomial fit ($y = a_0$

+a₁x+a₂x²; dy/dx = a₁ +2a₂x) such that. . .” this statement seems wrong to me. It implies that for every λ the expression $(a_1+2a_2\ln(\lambda))$ has the same value. Did you mean to write that Eq 5 is only valid for one λ ? That is λ_{ch} ?*

We appreciate this comment and have (we hope!) done a better job of explaining what we mean in this revision. After adding a sentence immediately after Eq. (5) in response to a comment from Referee #2, we revised the remainder of the text in the paragraph on lines 354-362 (441-450) as follows:

"For any given spectrum, there is one wavelength at which the linear and 2nd order polynomial fits yield equivalent results in Eq. (5). This must not be confused with every wavelength measured in the spectrum, so we will refer to this one wavelength as the characteristic wavelength of the measurement range, λ_{ch} , from here on. It can be calculated for each measured spectrum from the two sets of fit coefficients for that spectrum. That is, rewriting Eq. (5) in terms of λ_{ch} the characteristic wavelength of the measured spectrum may be calculated from $\lambda_{ch} = e^{((\alpha_{ext} + a_1) / -2a_2)}$. For the SpEx data set, λ_{ch} was found to range from 0.36 - 0.46 μm . In contrast, the empirical fit of $\alpha_{ext} = a_2 - a_1$ implies $\lambda_{ch} \sim 0.61$, i.e., $\ln(0.61) \sim -0.5$. The dependence of Eq. (5) on the characteristic wavelength, results in spectra sets with differing λ_{ch} exhibiting different mapping between α_{ext} and (a_1, a_2) . To illustrate this, consider the range of α_{ext} values (0.29 - 3.25) found from linear fits over 0.3 - 0.7 μm to all of the spectra measured by SpEx during KORUS-OC. This range of α_{ext} values maps differently into (a_1, a_2) space as a function of λ_{ch} (Fig. 9, top right panel)."

Line 357: "The wavelength dependence of Eq. (5)" if I understand correctly, Eq. 5 is not dependent on wavelength (i.e. the spectra of the measured data, 300-700 nm). It is dependent on the characteristic wavelength (λ_{ch}) as it is defined in the lines above.

Great catch! Thanks so much, we have revised this sentence as follows (and you will also have seen it in the revised paragraph included in the response to your comment above):

"The dependence of Eq. (5) on the characteristic wavelength, results in spectra sets with differing λ_{ch} exhibiting different mapping between α_{ext} and (a_1, a_2) ."

Line 360: did you mean figure 9? Not sure how figure 10 is related here.

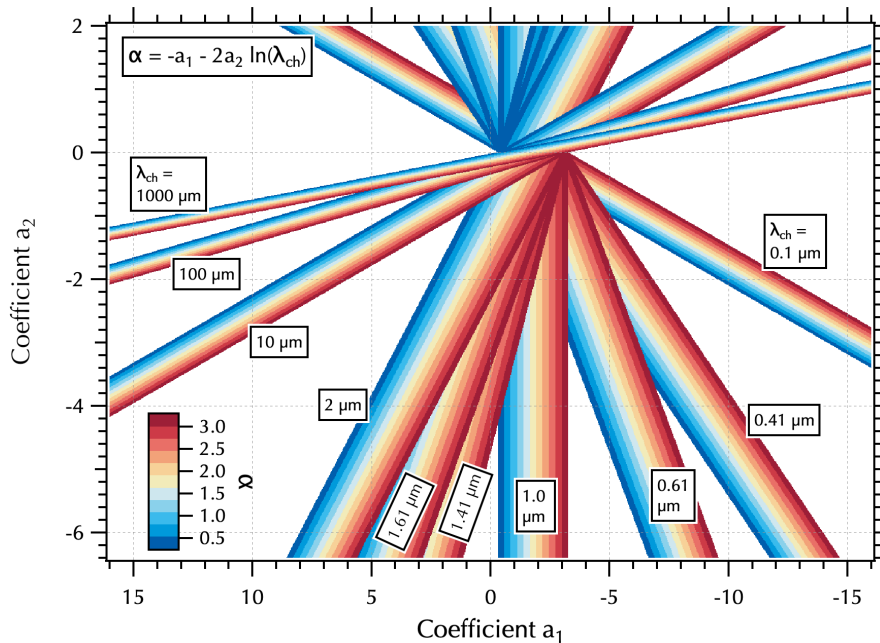
Yes, we did. Thanks for catching that typo on line 360 (450), it's fixed now.

Line 360-362: it is clear that when $a_2 = 0$ the 2nd order poly' fit is actually a line fit. What is the physical interpretation of $\lambda_{ch} = 1 \mu\text{m}$?

This is a great question! We have added two new paragraphs (starting at line 452 of the revised manuscript) to explain the implications of λ_{ch} and the special ("limiting" in the previous version wasn't quite the right word) cases immediately following the updated paragraph in response to your comment above regarding lines 350-355 of the submitted manuscript. We have also added Figure S8 to the supplement and include it here with the revised text for your convenience.

"There are two special cases evident in Eq. (5) that result in $\alpha_{\text{ext}} = a_1$. First, when there is no curvature ($a_2 = 0$), a_1 describes the same linear fit as α_{ext} . Second, when $\lambda_{\text{ch}} = 1 \mu\text{m}$ (i.e., $\ln(1) = 0$) Eq. (5) is insensitive to curvature such that a_2 can have any value at all. This can be understood from Eq. (1), where α can be any value when $\lambda = 1 \mu\text{m}$ and $p(1\mu\text{m})$ will always = β . The former leads to all λ_{ch} sets overlapping at $a_2 = 0$, while the latter exhibits a broad vertical band independent of curvature (a_2) (Fig. 9, top right panel). These special cases have important implications. As λ_{ch} approaches $1 \mu\text{m}$ the measurement becomes insensitive to curvature, while at the short wavelengths of light represented by $\lambda_{\text{ch}} < 0.1 \mu\text{m}$ the curvature itself becomes unimportant. Hence, to probe spectral curvature the upper right panel of Fig. 9 shows measurement techniques with $\lambda_{\text{ch}} \sim 0.5 \pm 0.2 \mu\text{m}$ provide the greatest sensitivity with sufficient separation in (a_1, a_2) to distinguish aerosol microphysical and chemical properties influencing the spectral shape.

The rotation as a function of λ_{ch} shown in Fig. 9 also illustrates why wavelength units of μm must be used to calculate (a_1, a_2) . As λ_{ch} increases to values $> 1 \mu\text{m}$, the α map rotates clockwise (Fig. S8). If one used $\lambda_{\text{ch}} = 410 \text{ nm}$ rather than $0.41 \mu\text{m}$, it would map into a narrow band in the next quadrant of (a_1, a_2) space spanning a wide range in a_1 but a narrow range in a_2 , resulting in little curvature sensitivity. The calculation of α_{ext} is wavelength independent and will produce the same result no matter what units are used. This is not the case for the calculation of (a_1, a_2) , so it must be emphasized that for curvature, the units matter."



"Figure S8. Illustration of the rotation of the mapping of α in (a_1, a_2) space as a function of λ_{ch} for long wavelengths. This illustration includes the extreme values of λ_{ch} of 100 and 1000 μm to stand in for the mapping that arises from using nm units instead of μm of wavelength."

Line 364: what does it mean?

This is now better explained in the new paragraphs provided in the response to the previous comment.

Line 369: to the right and left of which distribution?

We have revised the sentence on line 369 (502) to read:

"Note, that the most extreme values in a_1 for the KORUS-OC data set are related to shorter λ_{ch} than the rest of the data set."

Lines 376-378: "but as discussed. . .space". This section is really not clear. If the intension here was to link the information about the sampled aerosols that is available in other publications and that is presented in section 3.1 to the fitted parameter space, this is was not made clear. Please rephrase.

We have revised the text on lines 376-378 (508-511) as follows:

"Aerosol size distributions were not measured aboard ship during the cruise but as described in Sect. 3.1, previously published work provides sufficient information for a broad characterization of the different ambient aerosol populations prevalent during the three meteorological regimes that occurred during KORUS-OC. This context is used to assess the mapping of SpEx data into (a_1, a_2) space."

Figure 4 top: the gray trace is not visible.

As explained in the figure caption:

*"Top panel: SpEx (all data, gray; above LLOD, green; **these curves are coincident until June 2nd when the lowest values are below detection and hence, appear gray**)"*

There are very few spectra for which 532 nm σ_{ext} is below the LLOD, but for the smallest values in the time series after June 2nd, the reader will note that there are a few gray points visible below the majority of data in the time series in green.

Figure 6: it would be more intuitive for me to plot these data sets with the EAE calculated from the full range on x axis because this represents the optimal case and demonstrates the variances is most of the spectra to that case.

The choice of using 450-632 nm for the wavelength range on the x-axis is primarily intended for readers accustomed to α_{ext} values calculated from a few visible wavelengths from the sum of σ_{scat} and σ_{abs} measured with standard commercial instruments (e.g., similar to the NT σ_{ext} and NT α_{ext} in this work). Compared to values typically obtained from visible only wavelength ranges, α_{ext} values from the full SpEx wavelength range are smaller and this is the primary difference to which we want to draw the reader's attention.

Figure 7: what information is presented or made clearer in the top two figures that is not presented or is not clear in the middle two figures? In my opinion there is no add value to the top two and therefore should be removed. Additionally, the residual could be presented in relative terms (i.e. % error). This would be more intuitive to understand and reduce the text needed to describe the fit errors.

We feel that the top two panels of Fig. 7 are essential for providing context for the middle panels as discussed in the last 3 paragraphs of Section 3 starting at line 313 (398). Figure 7 is primarily for the benefit of those who by necessity extrapolate σ_{ext} into the UV from visible in situ measurements using α_{ext} to alert them to the potential for large errors. Further, Fig. 7 shows that extrapolating from 2nd order polynomials doesn't resolve this problem and therefore as the final sentence of Section 3 states:

"The divergence of either fit from the measured spectrum when extrapolating beyond the fit wavelength range (Fig. 7, middle panels) highlights the need for measurements across a broad spectral range in order to minimize the need for extrapolation."

Additionally, we use the residuals in this figure primarily to illustrate the improvement in the fit (i.e., the reduction in curvature in the top and bottom pair of panels) between the linear and 2nd order polynomials. Keeping the units the same between the main panel with the red spectrum and the black curve fit and the upper panel with the residuals is necessary to make this point.

Figure 8: here I would also suggest showing the x-axis in terms of relative error.

This figure is similar to one in Part 2 and both are intended to provide a means to illustrate that the improvement in the residuals from linear to 2nd order polynomial fits for the specific example spectra shown here in Fig. 7 here and in Fig. S4 of Part 2 apply to the data set as a whole. For this reason, we would prefer to keep the focus on the residuals rather than relative error in these figures.

Figure 9: in this figure all x-axis are inverted. This makes the figure less intuitive and harder to understand. Is there a reason for this choice? If yes I believe it should be explain in the text or at least in the figure caption. What is the purpose of the rectangle inset in the bottom panel of figure 9?

As discussed above the x-axes follow the previously published work of Schuster et al. (2006) to which we compare our results. We have updated the figure caption for Fig. 9 to conclude with the following explanation for the black box in the bottom panel:

"The black box is the same as the one in the top left panel."

Figure S2: it is not clear what this data set is based on. Is it simulation or measurements? If data is from another reference which is it?

This is a calculation. We have updated the figure caption as follows (note that this in now in reference to Fig. S3 due to the addition of the new Fig. S2):

"Figure S3. Illustration of the relationship between flow rate and size cut of the sampled aerosol particles based on theoretical calculations pertinent to the system deployed aboard the R/V Onnuri."

Figure S3: the full range of the right axis is not needed. Values range from 0 to 2.

The scale of the right axis was chosen to ensure that the black trace of the plume flag values did not interfere with the σ_{scat} and σ_{abs} curves above it.

Figure S4: what do the authors mean by hour set of intensity spectra? Is it a one hour average?

We have updated the figure caption as follows (again, note the updated figure number due to the new Fig. S2):

"Figure S5. Example of a one hour set of intensity spectra that illustrate the two wavelengths (332 nm and 467 nm) that sometimes saturated due to drift in the lamp intensity. 30 individual spectra measured at 2 min intervals over the course of one hour are shown. Typically (as is the case here) there is little discernible difference in intensity between sample and reference spectra over the full range of counts in the 16 bit spectrometer (0-65,536 counts)."

New In Situ Aerosol Hyperspectral Optical Measurements over 300-700 nm, Part 1: Spectral Aerosol Extinction (SpEx) Instrument Field Validation during the KORUS-OC cruise

Carolyn E. Jordan^{1,2}, Ryan M. Stauffer³, Brian T. Lamb⁴, Charles H. Hudgins², Kenneth L. Thornhill^{2,5},
5 Gregory L. Schuster², Richard H. Moore², Ewan C. Crosbie^{2,5}, Edward L. Winstead^{2,5}, Bruce E. Anderson²,
Robert F. Martin², Michael A. Shook², Luke D. Ziemba², Andreas J. Beyersdorf^{2,6}, Claire E. Robinson^{2,5},
Chelsea A. Corr^{2,7} and Maria A. Tzortziou^{3,4}

¹National Institute of Aerospace, Hampton, Virginia, United States of America

²NASA Langley Research Center, Hampton, Virginia, United States of America

10 ³NASA Goddard Space Flight Center, Greenbelt, Maryland, United States of America

⁴City University of New York, New York, New York, United States of America

⁵Science Systems and Applications Inc., Hampton, Virginia, United States of America

⁶California State University, San Bernardino, California, United States of America

⁷Springfield College, Springfield, Massachusetts, United States of America

15 *Correspondence to:* C. E. Jordan (Carolyn.Jordan@nasa.gov)

Abstract. In situ observations of spectrally-resolved aerosol extinction coefficients (300-700 nm at ~0.8 nm resolution) from the May-June 2016 Korea U.S. – Ocean Color (KORUS-OC) oceanographic field campaign are reported. Measurements were made with the custom-built Spectral Aerosol Extinction (SpEx) instrument that previously has been characterized only using laboratory-generated aerosols of known size and composition. Here, the performance of SpEx under realistic operating conditions in the field was assessed by comparison to extinction coefficients derived from commercial instruments that measured scattering and filter-based absorption coefficients at three discrete visible wavelengths. Good agreement was found between these two sets of extinction coefficients with slopes near unity for all 3 wavelengths within the SpEx measurement error ($\pm 5 \text{ Mm}^{-1}$). The meteorological conditions encountered during the cruise fostered diverse ambient aerosol populations with varying sizes and composition at concentrations spanning two orders of magnitude. The sampling inlet had a 50% size cut of 1.3 μm diameter particles such that the in situ aerosol sampling suite deployed aboard ship measured fine mode aerosols only. The extensive hyperspectral extinction data set acquired revealed that nearly all measured spectra exhibited curvature in logarithmic space, such that Ångström exponent (α) power law fits could lead to large errors compared to measured values. This problem was particularly acute for α values calculated over only visible wavelengths, then extrapolated to the UV, highlighting the need for measurements in this wavelength range. Second-order polynomial fits to the logarithmically-transformed data provided a much better fit to the measured spectra than the linear fits of power laws. Building on previous studies that used total column AOD observations to examine the information content of spectral curvature, the relationship between α and the second order polynomial fit coefficients (a_1 and a_2) was found to depend on the wavelength range of the spectral measurement such that any given α maps into a line in (a_1, a_2) coefficient space with a slope of $-2\ln(\lambda_{\text{ch}})$, where λ_{ch} is defined as the single wavelength that characterizes the wavelength range of the measured spectrum (i.e., the "characteristic wavelength"). Since the curvature coefficient values depend on λ_{ch} , it must be taken into account when comparing values from spectra obtained from measurement techniques with different λ_{ch} . Previously published work has shown that different bimodal size distributions of aerosols can exhibit the same α , yet have differing spectral curvature with different (a_1, a_2). This implies that (a_1, a_2) contain more information about size distributions than α alone. Aerosol size distributions were not measured during KORUS-OC and the data reported here were limited to the fine fraction, but the (a_1, a_2) maps obtained from the SpEx data set are consistent with the expectation that (a_1, a_2) may contain more information than α , a result that will be explored further with future SpEx and size distribution data sets.

1 Introduction

Significant natural variability in the size and composition of atmospheric aerosols introduces uncertainty into the representation of their optical properties and radiative impacts in models and satellite retrievals. While numerous airborne and surface-based observations over past decades have placed important constraints on these relationships, measurements have been typically limited to only one or a few wavelengths of light, which are extrapolated across the ultraviolet (UV)-visible-infrared (IR) spectrum by assuming a power law relationship (e.g., the well-known Ångström exponent). However, there is long standing evidence that extinction and aerosol optical depth spectra in the ambient atmosphere exhibit curvature that is not fully captured by a power law (e.g., King and Byrne, 1976; King et al., 1978; Kaufman, 1993; Reid et al., 1999; Eck et al., 1999, 2001a, b, 2003a, b; O'Neill et al., 2001; Schuster et al., 2006; Kaskaoutis et al., 2010, 2011; Rao and Niranjan, 2012). This wavelength-dependence of the aerosol extinction is thought to be driven primarily by the particle size distribution with only a minor contribution from the compositionally dependent aerosol absorption (Eck et al., 2001b; Schuster et al., 2006). However, these relationships remain largely qualitative and stem from columnar remote sensing measurements and Mie theory calculations. This motivates the incorporation of recently

Deleted: , especially in the ultraviolet (UV) wavelength range...

Formatted: Font: Symbol

Formatted: Subscript

Formatted: Subscript

Formatted: Font: Symbol

Deleted: shown to depend on the characteristic wavelength (λ_{ch}) of any given spectral measurement, such that differing curvature among aerosol size distributions with the same α will map to a line in (a_1, a_2) space with a slope related to λ_{ch} . Thus, ...

Deleted: represented

Deleted: by

Deleted:

Deleted: may provide more detailed aerosol size distribution ...

Formatted: Font: Symbol

Formatted: Font: Not Bold

developed, advanced instruments for measuring in situ, hyperspectral aerosol extinction into field campaigns that study the ambient atmosphere.

It is important to note that the power law assumption is empirical. Used to describe the interaction between light and aerosols (e.g. Ångström, 1989; Moosmüller and Chakrabarty, 2011),

$$p(\lambda) = \beta \lambda^{-\alpha} \quad (1)$$

p may represent various optical parameters of interest (e.g., scattering, absorption, extinction), λ is the wavelength of light (μm), β is p at 1 μm , and α is the Ångström exponent. One advantage of this representation is that the derivative of this relationship produces a line in logarithmic space with a wavelength-independent slope,

$$\alpha = -\frac{d \ln p(\lambda)}{d \ln \lambda} \quad (2)$$

Hence, from any 2 wavelengths, the Ångström exponent for the entire spectrum can be determined via

$$\alpha = -\frac{\ln(p(\lambda_2)/p(\lambda_1))}{\ln(\lambda_2/\lambda_1)} \quad (3)$$

The simplicity of this representation has led to its widespread use in the aerosol and remote sensing communities due to its utility in calculating $p(\lambda)$ at wavelengths for which there isn't a direct measurement. α is sensitive to the measurement error in $p(\lambda)$, such that if multiple wavelengths are available, it is preferable to perform a linear fit using Eq. (2) than a paired wavelength calculation as in Eq. (3). If the optical property of interest is fully described by a power law, then further spectral detail beyond several wavelengths is superfluous. However, if α is not, in fact, wavelength-independent for ambient aerosols, then a hyperspectral measurement (or sufficient wavelength sampling spanning the full wavelength range of interest) is required to capture the actual wavelength dependence.

Previous studies have considered various aerosol properties that may influence the spectral shape (and/or variation of the Ångström exponents calculated from different pairs of wavelengths) of ambient aerosol optical depth (AOD) such as the volume mean (or effective) radius of accumulation mode aerosols, the geometric standard deviation (i.e., width) of the accumulation mode, the volume fraction of the fine mode relative to the total aerosol population, and the absorption characteristics (i.e., composition) of the aerosol population (e.g., Reid et al., 1999; Eck et al., 1999, 2001b; Schuster et al., 2006). The relationships identified to date remain qualitative rather than quantitative and have been based on total atmospheric column measurements from remote sensors and on Mie calculations. Recently, the retrieval algorithm developed by O'Neill et al. (2001, 2003, 2008) to distinguish fine mode from coarse mode AOD components using 2nd order spectral fits has been applied to in situ extinction components based on scattering and absorption measurements made at a few visible wavelengths and evaluated using several sets of field data (Kaku et al., 2014, and references therein). The Spectral Aerosol Extinction (SpEx) instrument (Jordan et al., 2015) provides a new measurement approach that combines the advantages of a broad spectral range (typically limited to remote sensing techniques) with an in situ measurement capability (that allows for direct comparison to other in situ measurements of ambient aerosol microphysical and chemical properties). Combining this hyperspectral in situ measurement capability with retrieval techniques as in Kaku et al. (2014) also provides a new tool to fine tune remote sensing retrievals.

Although SpEx measures a narrower wavelength range (300 - 700 nm) than some remote sensors (e.g., ground-based 9 band sun-sky radiometers AERONET (340 - 1640 nm, Giles et al., 2019) and airborne hyperspectral sun-sky radiometer 4STAR (350 - 1750

Formatted: Superscript

Deleted: allows for similar analyses to be performed on ambient in situ measurements, but with greater spectral resolution (~0.8 nm) than has been available previously from the remote-sensing studies.

nm, 2 - 3 nm resolution, LeBlanc et al., 2020)) and similar ranges to others (e.g., hyperspectral polarimeters SPEX airborne (400 - 800 nm, 2 - 3 nm resolution in intensity, Smit et al., 2019; Fu et al., 2020) and SPEXone (385 - 770 nm, 2 nm resolution in intensity, Hasekamp et al., 2019) planned for the upcoming PACE mission (Werdell, et al., 2019; Remer et al., 2019a, 2019b)), it measures deeper into the UV range and has finer spectral resolution, ~0.8 nm. Similar in situ instruments, such as broadband cavity-enhanced spectroscopy (BBCES) instruments (e.g., Washenfelder et al., 2013, 2015; Bluvstein et al., 2016, 2017; He et al., 2018), do not provide as broad a UV-visible range as SpEx. Hence, SpEx is particularly suited to examine spectral details for ambient aerosols over its measurement range and to relate those spectral details to simultaneous in situ measurements of ambient aerosol microphysics and composition.

Previous work described SpEx using a series of laboratory tests that included a variety of non-absorbing and absorbing aerosols to characterize the instrument (Jordan et al., 2015). However, the purpose of SpEx is to measure atmospheric aerosols in the ambient environment. Hence, this manuscript is the first to offer details on the instrument performance in the field. The data presented here were obtained during the Korea United States - Ocean Color (KORUS-OC) oceanographic field campaign conducted around the Korean peninsula under the leadership of the Korean Institute of Ocean Science and Technology (KIOST) and the U.S. National Aeronautics and Space Administration (NASA). The KORUS-OC cruise was affiliated with the airborne KORUS - Air Quality (KORUS-AQ) campaign and the Korean Coastal water Ocean and Atmosphere (KOCOA) field campaign. These joint missions were conducted to study South Korean air quality and ocean color within the field of regard of South Korea's Geostationary Ocean Color Imager (GOCI) that provided hourly ocean color and aerosol optical depth (AOD) measurements. Although the primary scientific objectives of the KORUS-OC cruise focused on ocean color measurements (both in situ and remotely sensed), there were also objectives to address atmospheric correction requirements and to explore interdisciplinary science questions (e.g., Tzortziou et al., 2018; Thompson et al., 2019). The joint S. Korean and U.S. based science teams sailed aboard the KIOST research vessel *R/V Onnuri* (Fig. S1). Details on the scientific objectives of these field campaigns are provided in two white papers: Al Saadi et al. (2015) and US-Korean Steering Group (2015). An overview of the findings from KORUS-AQ is provided by Crawford et al. (2020) and references therein.

Two commercial instruments (AirPhoton's integrating nephelometer, IN101, and Brechtel's Tricolor Absorption Photometer, TAP) were also deployed to measure in situ aerosols at three visible wavelengths providing scattering coefficients and absorption coefficients, respectively. These measurements are presented in detail here and used to evaluate the performance of SpEx. Filter samples were also collected and analyzed in the laboratory for spectral absorption and chemical composition as discussed in Part 2 of this work. Those data provide additional context for the measurements described here in Part 1. Further, Part 2 presents an assessment of the applicability of a methodology routinely used by the ocean color community to measure hyperspectral particle absorption for use with ambient atmospheric aerosol samples. Hence, Part 2 includes further discussion of the ability of power laws to fully represent the observed hyperspectral variability of in situ aerosol optical properties as measured during KORUS-OC.

2 Methods

2.1 Ship deployment

The measurements reported here from 20:25 May 21 through 09:00 June 4, 2016 Korean Standard Time (KST, KST = UTC + 9) were made outside of South Korea's territorial seas (> 12 nautical miles, 22.2 km, from the coast, Fig. 1, top left panel). The

Deleted: view

Deleted: .

instrument suite (Fig. S2) was deployed above the bridge strapped to the starboard rail in a custom-built box designed to keep the instruments dry yet ventilated to prevent overheating (Fig. S1). The pumps were located in a separate box a few meters away tied to the stern rail (Fig. S1) to limit thermal and mechanical interference with the measurements. Measurements were made at ambient temperature (T), pressure (P), and relative humidity (RH) (i.e., the aerosols were not dried prior to measurement) with the exception of the TAP instrument which is internally heated and kept at a constant 35 °C. T, P, and RH were measured both aboard ship and within the sampling system. Although the sampling box was ventilated, it was not climate controlled. On the top deck it was in direct sunlight during the day and even at night various components in the system kept the interior warmer and drier than ambient air. These conditions led to diurnal variability in the difference between sampling and ambient conditions, such that the sampling T was ~ 6 °C warmer at night increasing to as much as ~15 °C warmer in mid-afternoon. Similarly, ambient RH ranged from 55 - 98% RH throughout the cruise, while the sampling RH ranged from ~ 30 - 70%. For the purposes of this work (both Parts 1 and 2), the comparisons made are all within this sampling system with T and RH consistent across all measurements, except for TAP. Since non-volatile black carbon (BC) is expected to dominate the absorption measurement, this difference is expected to have a limited impact on the results. The primary objective in this work is to evaluate the performance of SpEx by direct comparisons to the data from the two commercial instruments in the measurement suite. Hence, we did not perform any corrections to either ambient T and RH or to standard temperature and pressure (STP) prior to comparing these data. There are no comparisons in this pair of manuscripts to other data sets, so such corrections are not necessary for this study.

Deleted: measurement package

Deleted: ,

Deleted: Hence, all data are reported here at sampling T and RH...

The available berths aboard ship constrained the number of personnel available to operate the sampling system, so it was necessary to configure the system to operate nearly autonomously. To ensure that water did not enter the sampling line, a tall stainless steel sampling mast (19.05 mm (3/4") inner diameter tubing) was used to minimize the chance of sea spray entering the line from below. Further, the inlet was attached to the vertical sampling mast with a curved section of stainless steel tubing such that the inlet was downward facing to prevent any potential precipitation from entering the line from above as well (Fig. S1). This configuration worked as intended with the inlet approximately 10 m above the sea surface. However, the fast flow rate required for the SpEx measurement (approximately 70 lpm) through the curved inlet resulted in the removal of coarse aerosol with a 50% size cut of ~1.3 μm diameter (Fig. S3). Hence, all of the measurements here (sampling from the same inlet, Fig. S2) reflect only the fine fraction aerosol in the marine boundary layer (MBL).

Deleted: S2

Deleted: off

Deleted: line

While the SpEx and commercial instruments were run mostly uninterrupted, colleagues from other groups aboard ship carried out the routine filter changes needed throughout the cruise. They also ensured that the system ran properly and were there to handle problems. The methodology and results of the filter sampling will be presented in the companion paper (Part 2, Jordan et al., 2020b).

Deleted: , especially at the end of the cruise when the instrument box came loose and lost power in stormy weather with rough seas on the morning of June 4th

Deleted: As the ship was on its way back to port and rain limited the value of restarting the system, measurements from this suite of instruments ended at that time.

Deleted: wo commercial

Deleted: with

Deleted: instruments deployed for this purpose were Brechtel's Tricolor Absorption Photometer (

Deleted: ; <https://www.brechtel.com/products-item/tricolor-absorption-photometer>

Deleted: with 1 s measurement resolution

Deleted: AirPhoton's Integrating Nephelometer model 101 (...)

Deleted: ; <https://www.airphoton.com/nephelometers.html>

Deleted: with ~10 s resolution

2.2 Aerosol scattering and absorption coefficient measurements and derived parameters

The IN101 and TAP instruments provide data at a higher temporal resolution than SpEx and were deployed with two objectives: 1) to identify and flag incidents of ship exhaust ("plume") contamination of the data set, and 2) to evaluate the new spectral measurements (both from SpEx and the filters). The TAP (model 2901, Brechtel, Hayward, CA) measures absorption coefficients (σ_{abs}) at 467, 528, and 652 nm with 1 s resolution and the IN101 (AirPhoton, Baltimore, MD) measures scattering coefficients (σ_{scat}) at 450, 532, and 632 nm with ~10 s resolution.

To identify ship plume interceptions, an initial examination of the IN101 σ_{scat} and TAP σ_{abs} data was performed. One-minute averages were calculated in order to calculate the single scattering albedo ($\omega = \sigma_{\text{scat}} / (\sigma_{\text{scat}} + \sigma_{\text{abs}})$). The σ_{scat} data was corrected using the submicron factors in Anderson and Ogren (1998). These corrections are needed to resolve truncation errors in the forward scattering (the 7° to 0° range missing from the measurement) and non-Lambertian errors that arise from the distribution of light by the opal glass diffusor. Due to limited personnel, calibrations were not performed during the cruise. Pre- and post-cruise calibrations using pure CO₂ were performed in the laboratory to correct the final archived data and indicate the instrument performance was stable throughout the measurement period. The σ_{abs} data was corrected for scattering as recommended in Ogren et al. (2017).

Interception of the ship plume was first identified using one-minute averages of the gas-phase NO₂ and O₃ measurements (Thompson et al., 2019). The inlets for the gas-phase instruments were near, but not co-located with the aerosol inlet, so the one-minute averages of ω , σ_{abs} , and σ_{scat} were used to further assess evident ship plume interceptions in the aerosol data set. The σ_{abs} data were particularly sensitive to such interceptions exhibiting dramatic brief spikes in the otherwise smoothly varying time series (the interested reader can compare σ_{abs} in Fig. S4 that shows all of the data in the time series including ship plume interceptions to σ_{abs} in the top panel of Fig. 2 where the plume interceptions have been removed). These were easily identifiable and removed manually. The inlets for the in situ instruments were towards the starboard bow (gas-phase on a lower deck, a few meters aft of the aerosol inlet) opposite of the ship stack pointed toward the port side stern. While underway, ship plumes did not affect the measurements, but they were encountered occasionally when on station or, as was more frequently the case, when getting underway from a stationary sampling site. The archived plume flags (= 0 for ambient air, 1 for ship plume interceptions) may be used to either remove data points affected by ship contamination or to assess ship plume contamination of filter samples (see Part 2).

In addition to the 1 min averaged σ_{scat} and σ_{abs} data reported in the KORUS-AQ data archive, averages were also calculated for each 30 s SpEx sampling interval and corrected in the same manner as the 1 min data set. The IN101 and TAP instruments measure at different wavelengths, so in order to calculate σ_{ext} ($= \sigma_{\text{scat}} + \sigma_{\text{abs}}$), the TAP data were adjusted to the IN101 wavelengths using Eq. (3). For clarity, these extinction coefficients are denoted NT (for Nephelometer + TAP) σ_{ext} in comparison to the measured SpEx σ_{ext} at those wavelengths (450, 532, and 632 nm). Similarly, a second set of plume flags was created for the SpEx sampling interval (i.e., based on plume interceptions for 30 s intervals approximately every 4 minutes, see Sect. 2.3).

2.3 Spectrally-resolved aerosol extinction coefficient measurements

Developed from a prototype described in Chartier and Greenslade (2012) SpEx is described in detail in Jordan et al. (2015). SpEx is a White-type optical cell (White, 1942) with a 39.4 m path length and a 17 l internal volume. A flush time of 90 s completely exchanges the air in the cell (3 times the volume) for flow rates > 34 lpm, here, the flow rate was ~70 lpm. The optical cell is coupled via fiber optics to a UV5000 system (Cerex Monitoring Solutions, LLC, Atlanta, GA) with a 150 W xenon lamp source (Cerex P/N CRX-X150W), integrated with an Ocean Optics, Inc. (Dunedin, FL) QE65Pro 16-bit spectrometer. Sampling for 30 s using an integration time of ~20-50 ms optimizes the signal to noise ratio for each measured intensity spectrum (Jordan et al., 2015). An automated valve system controls the 4-minute sampling cycle by switching the flow between the filtered line (ambient air without aerosols) and an unfiltered line (ambient air with aerosols): 90 s flush, 30 s sample without aerosols, 90 s flush, 30 s sample with aerosols, repeat.

Deleted: scattering coefficient (

Deleted:)

Deleted: absorption coefficient (

Deleted:)

Deleted: S3

Deleted: As

Deleted: ,

The intensity spectrum is measured for the sample without aerosols for a reference ($I_0(\lambda)$) and for the sample with aerosols ($I(\lambda)$) from which the extinction spectra ($\sigma_{\text{ext}}(\lambda)$) are calculated using the extinction law (Eq. (4)),

$$\sigma_{\text{ext}}(\lambda) = \frac{-\ln(I(\lambda)/I_0(\lambda))}{L} \quad (4)$$

where λ is the wavelength of light and L is the optical path length (here, in units of Mm). Hence, extinction spectra are acquired every 4 minutes. Reference spectra before and after each sample spectrum are averaged together to account for drift in the intensity between measurements in the calculation of σ_{ext} . A particular strength of this measurement is it explicitly accounts for extinction arising from gas-phase constituents via the reference spectra. No calibrations are needed to obtain aerosol σ_{ext} . Laboratory tests have shown the measurement error over the full spectral range of the measurements (300-700 nm) to be about $\pm 5 \text{ Mm}^{-1}$ (Jordan et al., 2015).

Several modifications have been made to the instrument since the laboratory studies reported in Jordan et al. (2015). These include an automated switching system between valves that control flow between filtered and unfiltered air and new custom control software that allows for continuous unattended operation. Further, the metal-jacketed optical fibers used previously were replaced with bare optical fibers securely packed in foam to reduce noise when deployed on mobile platforms. This last change resulted in greatly improved data quality with far fewer spectra disrupted due to mechanical disturbance under field conditions. Nonetheless, some spectra had to be rejected from the final data set due to features that provided clear evidence of disturbance. Typically, this occurred around the times of the filter changes when the lid of the box housing the sampling system needed to be raised to change filters (flagged using the plume flag field, value set to 2, see Fig. S4). Sometimes the filters were changed during flush times, leaving measured spectra unaffected, while at other times, disturbed spectra persisted for some period of time around the filter change. This suggests other vibrations arising from work involving nearby instruments or elsewhere on the ship may have contributed to the noisy rejected spectra. More work is required to further reduce the susceptibility of SpEx to sources of vibrational noise; nonetheless $< 8\%$ of the 4255 measured spectra were rejected from the data set overall. Note, ship plume interception (affecting $< 6\%$ of the measured spectra) often resulted in distorted spectra likely due to rapid changes in both the aerosol population and the gas-phase concentrations used to establish the reference spectrum for the calculation of aerosol extinction as in Eq. (4). Hence, only spectra obtained when the plume flag = 0 should be used for analysis of ambient conditions.

One consequence of unattended operation is the intensity drift sometimes resulted in saturated pixels around 332 nm and 467 nm due to peaks at those wavelengths in the lamp spectrum (Fig. S5). Saturation can be prevented either by adjusting the integration time of the spectrometer or by realigning the optics. However, unattended operation necessitated filtering the spectra at those two wavelengths when saturation occurred. The 16-bit spectrometer has a maximum intensity count of 65,536 (2^{16}), however, saturation effects became apparent before reaching this maximum. Tests showed that a threshold of 63,000 counts was a suitable limit for removing saturation effects from the spectrum. Filtering the 467 nm channel and the two adjacent pixels on either side of that channel removed the saturation distortions completely. The saturation effects at 332 nm were filtered in the same way, however, there appeared to be a minor shoulder effect that extended over a broader wavelength range in the UV. The effect was minimal (a few percent of the measured value) and well within the measurement error. However, caution is recommended against over-interpreting the shape of a spectrum in the vicinity of 332 nm when the saturation flag (Sat332Flag) for this channel is set to 1. Saturation at 332 nm affected 16% of the total 4255 measured spectra.

Deleted: S3

Deleted: S4

3 Results

3.1 Overview of σ_{scat} and σ_{abs} during KORUS-OC

Four distinct synoptic meteorological regimes have been described in detail for the KORUS-AQ period (Peterson et al., 2019). The KORUS-OC cruise departed the peninsula (Fig. 1, top left panel) sailing to the East Sea (Sea of Japan) near the end of the 2nd of these periods, the Stagnant period, characterized by limited transport and enhanced photochemical production of secondary organic aerosols (Kim et al., 2018; Nault et al., 2018; Choi et al., 2019; Jordan et al., 2020a). This regime started breaking down on May 23rd, followed by a precipitation event on the 24th that reduced ambient aerosols to low concentrations as reflected by low (tens of Mm^{-1}) σ_{scat} (Fig. 2, top panel).

From May 25th through the 31st the Transport/Haze period was characterized by air mass transport (from the west/northwest carrying pollutants from China), overcast hazy conditions, and rapid local South Korean secondary production of inorganic aerosols resulting in the largest concentrations of the $\text{PM}_{2.5}$ fraction of aerosols (i.e., particulate matter with diameters $\leq 2.5 \mu\text{m}$) observed during the KORUS-AQ campaign (Peterson et al., 2019; Eck et al., 2020; Jordan et al., 2020a). The greatest σ_{scat} values (hundreds of Mm^{-1}) observed aboard the R/V Onnuri were found during the first half of the Transport/ Haze period while the ship was downwind of the Korean peninsula in the East Sea (Fig. 1, top panels, and Fig. 2, top panel). Lower σ_{scat} values were observed during this period when the ship was upwind of the peninsula following its transit to the West Sea (Yellow Sea).

The final of the four synoptic periods, the Blocking period, followed a frontal passage that ended the previous Transport/Haze period (Peterson et al., 2019). This final frontal passage swept in cleaner air from the north leading to a rapid decrease in aerosol concentrations reflected in the reduced σ_{scat} observed aboard ship (Fig. 2). The Blocking period was then characterized by limited transport and occasional brief stagnant periods due to adjacent high and low pressure systems with the high poleward of the low (called a Rex Block). Under these conditions, local sources dominated pollutants, but aerosols did not accumulate to large concentrations (Peterson et al., 2019; Jordan et al., 2020a). This led to strikingly low σ_{scat} values (tens to $< 10 \text{ Mm}^{-1}$, Fig. 2), even lower than those observed during the precipitation event on May 24th.

Throughout the cruise σ_{abs} values were typically an order of magnitude smaller than σ_{scat} (Fig. 2, top panel) with peak values generally found at the same locations and times as peak σ_{scat} (Fig. 1). Hence, while the temporal variability of σ_{abs} largely followed σ_{scat} , the range in the magnitude of σ_{abs} ($0.36 - 18.07 \text{ Mm}^{-1}$) at 532 nm was far less than that of σ_{scat} ($2.8 - 332.2 \text{ Mm}^{-1}$). This led to the finding that single scattering albedo values ($\omega(\lambda) = \sigma_{\text{scat}}(\lambda) / \sigma_{\text{ext}}(\lambda)$) were driven by the change in scattering not absorption. Typically, ω was > 0.9 (Fig. 1, bottom right panel, and Fig. 2, bottom panel). The excursions below this value observed on May 23rd and 24th occurred when the reduction in σ_{scat} exceeded that observed in σ_{abs} .

The most extreme low values of ω (~ 0.7 for 532 nm, Figs. 1 and 2), however, occurred during the Blocking period, when the temporal evolution of σ_{abs} did not closely follow σ_{scat} . At that time, the scattering Ångström exponents (α_{scat}) increased to values > 3 , while absorption Ångström exponents (α_{abs}) were ~ 1 (Fig. 2, middle panel). These data indicate that the aerosol population was dominated by small particles, likely black carbon (BC). The temporal evolution of carbon monoxide (CO, Fig. 2, bottom panel) and σ_{scat} (Fig. 2, top panel) were strikingly similar from 04:00 June 1st through 20:00 June 2nd, exhibiting an $r^2 = 0.841$ for a linear regression over that time. This is in contrast to the Blocking period as a whole ($r^2 = 0.514$) or the rest of the campaign,

Deleted: ,

Deleted: where

335 excluding the Blocking period ($r^2 = 0.623$). The good correlation with CO, the BC signature in α_{abs} , the small particle population indicated by α_{scat} , and the limited transport of the Blocking period, together suggest that the low ω values arose from local ship emissions either from commercial or fishing vessels or both. Note, the inference that aerosols during the Blocking period were from local ship emissions refers to the regional ambient environment and should not be confused with ship plume contamination from the R/V Onnuri (see Section 2.2 for the criteria used to remove ship stack contamination from the data set).

Formatted: Font: Italic

340 Aside from the Blocking period, α_{scat} typically ranged from $\sim 1.5 - 2$, with evident wavelength dependence in the α_{scat} wavelength pairs (Fig. 2, middle panel). Little difference was found among the wavelength pairs in the α_{abs} values that typically ranged from $\sim 0.5 - 1$ throughout the cruise.

3.2 Comparison of SpEx data to σ_{ext} calculated from $\sigma_{\text{scat}} + \sigma_{\text{abs}}$

345 σ_{ext} calculated from the $\sigma_{\text{scat}} + \sigma_{\text{abs}}$ data (denoted NT σ_{ext} to distinguish it from SpEx σ_{ext}) averaged over the SpEx sampling intervals (see Sect. 2.2) were compared to the 450, 532, and 632 nm channels of SpEx (Fig. 3). Excellent agreement was found with slopes of 1.020 ± 0.002 , 0.998 ± 0.003 , and 1.057 ± 0.004 for all of the data in each of the three channels (gray plus markers in all panels of Fig. 3), respectively. Three intervals were used to look at mean comparisons: 15 min (light colored circles), 30 min (dark colored triangles), and 60 min (black diamonds). The slopes, intercepts, and r^2 values for all of the fits are shown in Fig. 3. These fits were performed using data limited to the valid measurement range (i.e., above the lower limit of detection, LLOD). Tests indicated that a limit of twice the measurement uncertainty provided a suitable LLOD (10 Mm^{-1}).

350 The SpEx data were more variable than the NT σ_{ext} as is evident in time series comparisons throughout the cruise (Figs. 4, S6, and S7, top panel). This is partly attributable to the differing noise characteristics of the measurement techniques, but it also arises from differences in sampling intervals where the standard error of the means reduces the variability by the square root of the number of samples in the mean. The NT σ_{ext} represent 30 s means calculated from $\sim 10 \text{ s}$ σ_{scat} and 1 s σ_{abs} measurements for each SpEx σ_{ext} spectrum. Averaging SpEx σ_{ext} reduces the variability (Figs. 4, S6, and S7, middle panel) according to the standard error of the means. However, not all of the variability evident in Fig. 4 is noise. Limiting the data range in the time series to 2 days (Fig. 5) illustrates that the native resolution of SpEx captured rapid changes that were also evident in the NT data. For example, consider the double peak feature that occurred around 03:00 on May 25th (top panel, Fig. 5). This temporal variation is lost even in the 15 min average (bottom panel, Fig. 5).

Deleted: S5

Deleted: S6

Deleted: largely

Deleted: .

Deleted: S5

Deleted: S6

360 For clarity, the standard deviations for the means are shown separately (Figs. 4, S6 and S7, bottom panels). Most of the standard deviations of the means in these channels were consistent with the measurement error of about $\pm 5 \text{ Mm}^{-1}$ with larger values arising from changes in the ambient conditions. Hence, the standard deviations of the 60 min means describe an upper envelope compared to the 15 and 30 min means as changing ambient conditions led to greater variability in the means. Together, the results shown in Figs. 3-5 show that quantitative data were obtained under field conditions with SpEx at its native sampling resolution.

Deleted: S5

Deleted: S6

3.3 Evaluating extinction Ångström exponents (α_{ext}) with hyperspectral extinction data

365 With the spectral data available from SpEx, it was possible to test the power law behavior of the individual and mean spectra by fitting a line to each spectrum in logarithmic space per Eq. (2), where the Ångström exponent, α_{ext} is the negative value of the slope. As discussed in the introduction, if a power law described the relationship well, α_{ext} should be invariant with wavelength.

380 Yet clear separation was found in α_{ext} from linear fits to all of the individual spectra (All Data, Fig. 6, left panel) depending on the wavelength range used for the fit. The α_{ext} from fits to the full range (300-700 nm), and two partial ranges (450-532 nm) and (532-632 nm) deviate from the 1:1 line expected when plotted vs. α_{ext} from fits to the 450-632 nm range. This result was also found for α_{ext} determined from all of the mean spectra sets as well (e.g., those from the 30 min mean spectra, right panel Fig. 6).

385 Most of the SpEx spectra measured during the cruise exhibited curvature over the 300-700 nm range in logarithmic space. Note, in order to compare results here to previously published work (Sect. 4), for the remainder of this section fits will be shown using wavelength in units of μm . This change in units does not alter the values of α_{ext} (which are invariant with wavelength and hence, the choice of units does not matter), but it does change the other coefficients from the mathematical fits to the spectra as will be discussed further in Sect. 4. An example of the observed curvature is provided in Fig. 7. The measured spectrum shown (red curve, Fig. 7, all panels) is curved such that residuals (the difference between the measured spectrum and the mathematical fit, blue curves) from the linear fits (black lines, left panels) are also curved. If a particular mathematical function (here, a power law) provides a good fit to the data, the residuals should be randomly distributed around zero. If there is a trend (the curvature evident here), then other functions should be considered to see if a better fit may be obtained. The curvature in the residuals is evident not only across the full wavelength range (Fig. 7, bottom left panel), but for subsets of that range as well (e.g., the 0.45 - 0.632 μm fit, Fig. 7, top left panel). Note, the log scale used to plot the spectrum (red curves) in Fig. 7 along with the relatively small extinctions at long wavelengths exaggerates the appearance of noise at those wavelengths (i.e., $\pm 5 \text{ Mm}^{-1}$ at the red end where $\sigma_{\text{ext}} \sim 20 \text{ Mm}^{-1}$, $\text{LN}(20) \sim 3$, is more obvious than in the UV where $\sigma_{\text{ext}} \sim 150 \text{ Mm}^{-1}$, $\text{LN}(150) \sim 5$). Nonetheless, the intensity of the xenon lamp decreases from 600 to 700 nm (Fig. S5; in Fig. 7, $\text{LN}(0.6 \mu\text{m}) \sim -0.51$, $\text{LN}(0.7 \mu\text{m}) \sim -0.36$) such that smaller values of I_0 combined with the small differences between I and I_0 in this wavelength range lead to slightly greater uncertainty in σ_{ext} (Eq. (4)).

395 The wavelength dependent curvature can lead to large errors if used to extrapolate to wavelengths beyond the measured range of values. For example, using α_{ext} found from the 0.45-0.632 fit to extrapolate to 0.3 μm (Fig. 7, middle left panel) leads to a value of $\text{LN}(\sigma_{\text{ext}}) = 5.7099$, while the measured value was 5.0839, i.e., an extrapolated extinction of 302 Mm^{-1} , 87% larger than the measured extinction of 161 Mm^{-1} . This wavelength is the most extreme, but the positive artifact is present throughout the UV range: with the extrapolated extinction 73% and 29% greater at 0.315 and 0.365 μm , respectively. At 0.45 μm ($\text{LN}(0.45 \mu\text{m}) = -0.8$, Fig. 7), the lower end of the fit range of values, the fit extinction was 6% greater than the measured value, while at 0.532 μm (the middle of the fit range) it was 3% less.

405 Previous work has shown that 2nd order polynomials in logarithmic space can provide a better fit to ambient aerosol optical depth (AOD, aerosol extinction integrated over an atmospheric column) spectra than power law fits (e.g., Eck et al., 1999, 2001a, b, 2003a, b; Schuster et al., 2006; Kaskaoutis et al., 2010, 2011). In the example shown in Fig. 7, it is clear that a 2nd order polynomial fit (black curves, right panels) reduces the trends in the residuals both over the full wavelength range (bottom right) and over the 0.45-0.632 μm subset of that range (top right) from that obtained from the linear fits. The improved fit provided by a 2nd order polynomial for all of the measured spectra is shown using histograms of the residuals at 6 wavelengths across the measured wavelength range (Fig. 8). For both the linear fits (black bars) and the 2nd order polynomial fits (red bars), the range of values for residuals at each wavelength is divided into 20 bins. The narrower bins for the 2nd order polynomial fits reflect the smaller range in residual values compared to those from the linear fits. The best agreement between the two sets of residuals shown in Fig. 8 is found at 0.532 μm , where the linear fit residuals are distributed around zero. At longer and shorter wavelengths, however, the linear residuals tend to be either positive or negative at any given wavelength, while the 2nd order polynomial fit residuals are

Deleted: that will be discussed.

Formatted: Superscript

Formatted: Font: 10 pt, Not Italic

Formatted: Font: 10 pt, Not Italic

Formatted: Font: 10 pt, Not Italic

Formatted: Font: 10 pt, Not Italic

Formatted: Font: 10 pt, Not Italic

Formatted: Font: 10 pt, Not Italic

Deleted: is

centered around zero across all wavelengths. These results confirm that 2nd order polynomials provide a better fit to the data than linear fits.

Unfortunately, just as extrapolating linear fits beyond the measurement range is problematic, the same is also true for the 2nd order polynomial fits (Fig. 7, middle right panel). In this case, at 0.45 and 0.532 μm (within the fit range) the fit agrees with the measured extinctions within 1% (~ 85 and 56 Mm^{-1} , respectively). However, at increasingly shorter wavelengths the fit diverges from the measured spectrum with the fit values 15%, 28%, and 34% too small at 0.365, 0.315, and 0.3 μm , respectively. The divergence of either fit from the measured spectrum when extrapolating beyond the fit wavelength range (Fig. 7, middle panels) highlights the need for measurements across a broad spectral range in order to minimize the need for extrapolation.

4 Discussion

The motivation to fit the SpEx spectra with a 2nd order polynomial came primarily from the work of Schuster et al. (2006) in which both Mie calculations and AERONET data were used to explore the additional information that spectral curvature may provide. A comparison of the coefficients obtained from SpEx to the fine fraction subset of aerosols reported in Schuster et al. (2006) revealed two key differences between the data sets. First, the a_1 and a_2 coefficients spanned a wider range of values than those obtained in the prior work (Fig. 9, top left panel). Second, Schuster et al. (2006) reported an empirical approximation such that α_{ext} was approximately equal to $a_2 - a_1$. This approximation clearly does not hold for the values obtained from this data set (Fig. 9, top left panel). These differences can be understood as follows.

The two expressions used here to fit the relationship between σ_{ext} and λ are related by their negative derivative, defined as α in Eq. (2). That is, the derivative of the linear fit ($y = a + bx$; $dy/dx = b$) equals the derivative of the 2nd order polynomial fit ($y = a_0 + a_1x + a_2x^2$; $dy/dx = a_1 + 2a_2x$) such that

$$\alpha_{\text{ext}} = -b = -(a_1 + 2a_2(\ln(\lambda))) \quad (5)$$

Note, the derivative of Eq. (5), $d\alpha_{\text{ext}}/d\ln(\lambda) = -2a_2$ defines the curvature of the extinction spectra (Eck et al., 1999). For any given spectrum, there is one wavelength at which the linear and 2nd order polynomial fits yield equivalent results in Eq. (5). This must not be confused with every wavelength measured in the spectrum, so we will refer to this one wavelength as the characteristic wavelength of the measurement range, λ_{ch} , from here on. It can be calculated for each measured spectrum from the two sets of fit coefficients for that spectrum. That is, rewriting Eq. (5) in terms of λ_{ch} the characteristic wavelength of the measured spectrum may be calculated from $\lambda_{\text{ch}} = e^{-(\alpha_{\text{ext}} + a_1) / -2a_2}$. For the SpEx data set, λ_{ch} was found to range from 0.36 - 0.46 μm . In contrast, the empirical fit of $\alpha_{\text{ext}} = a_2 - a_1$ implies $\lambda_{\text{ch}} \sim 0.61$, i.e., $\ln(0.61) \sim -0.5$. The dependence of Eq. (5) on the characteristic wavelength, results in spectra sets with differing λ_{ch} exhibiting different mapping between α_{ext} and (a_1, a_2). To illustrate this, consider the range of α_{ext} values (0.29 - 3.25) found from linear fits over 0.3 - 0.7 μm to all of the spectra measured by SpEx during KORUS-OC. This range of α_{ext} values maps differently into (a_1, a_2) space as a function of λ_{ch} (Fig. 9, top right panel).

There are two special cases evident in Eq. (5) that result in $\alpha_{\text{ext}} = a_1$. First, when there is no curvature ($a_2 = 0$), a_1 describes the same linear fit as α_{ext} . Second, when $\lambda_{\text{ch}} = 1 \mu\text{m}$ (i.e., $\ln(1) = 0$) Eq. (5) is insensitive to curvature such that a_2 can have any value at all. This can be understood from Eq. (1), where α can be any value when $\lambda = 1 \mu\text{m}$ and $p(1 \mu\text{m})$ will always = β . The former leads to all λ_{ch} sets overlapping at $a_2 = 0$, while the latter exhibits a broad vertical band independent of curvature (a_2) (Fig. 9, top

- Deleted: os
- Formatted: Font: Symbol
- Deleted: Hence, f
- Formatted: Subscript
- Formatted: Font: Symbol
- Formatted: Subscript
- Formatted: Font: Times New Roman, Subscript
- Formatted: Font: Symbol
- Formatted: Font: Times New Roman
- Deleted: a
- Deleted: his wavelength (called the
- Deleted:)
- Deleted: each
- Formatted: Font: Symbol
- Formatted: Subscript
- Formatted: Subscript
- Formatted: Subscript
- Deleted: .
- Deleted: wavelength
- Deleted: 10
- Deleted: limiting
- Deleted: where
- Deleted: :
- Deleted: either
- Formatted: Subscript
- Formatted: Font: Symbol
- Formatted: Subscript
- Deleted: (i.e., no curvature in the spectrum) o
- Deleted: r
- Formatted: Subscript
- Formatted: Font: Symbol
- Formatted: Font: Symbol
- Formatted: Font: Symbol

right panel). These special cases have important implications. As λ_{ch} approaches $1 \mu\text{m}$ the measurement becomes insensitive to curvature, while at the short wavelengths of light represented by $\lambda_{\text{ch}} < 0.1 \mu\text{m}$ the curvature itself becomes unimportant. Hence, to probe spectral curvature the upper right panel of Fig. 9 shows measurement techniques with $\lambda_{\text{ch}} \sim 0.5 \pm 0.2 \mu\text{m}$ provide the greatest sensitivity with sufficient separation in (a_1, a_2) to distinguish aerosol microphysical and chemical properties influencing the spectral shape.

The rotation as a function of λ_{ch} shown in Fig. 9 also illustrates why wavelength units of μm must be used to calculate (a_1, a_2) . As λ_{ch} increases to values $> 1 \mu\text{m}$, the α map rotates clockwise (Fig. S8). If one used $\lambda_{\text{ch}} = 410 \text{ nm}$ rather than $0.41 \mu\text{m}$, it would map into a narrow band in the next quadrant of (a_1, a_2) space spanning a wide range in a_1 but a narrow range in a_2 , resulting in little curvature sensitivity. The calculation of α_{ext} is wavelength independent and will produce the same result no matter what units are used. This is *not* the case for the calculation of (a_1, a_2) , so it must be emphasized that for curvature, the units matter.

The angular difference between $\lambda_{\text{ch}} = 0.61 \mu\text{m}$ and $0.41 \mu\text{m}$ accounts for the shift between the mapping reported in Schuster et al. (2006) and this work. The differing values in λ_{ch} arise from the different spectral ranges between AERONET (7 bands spanning $0.34 - 1.02 \mu\text{m}$, Schuster et al. (2006)) versus $0.3 - 0.7 \mu\text{m}$ for SpEx. The α_{ext} values from fits to the spectra set map into the expected bands (Fig. 9, bottom panel) with the color distribution shifting slightly over the range of calculated $\lambda_{\text{ch}} = 0.36 - 0.46 \mu\text{m}$. Note, that the most extreme values in a_1 for the KORUS-OC data set are related to shorter λ_{ch} than the rest of the data set.

Schuster et al. (2006) used this type of coefficient mapping to distinguish different aerosol size distributions via curvature that otherwise exhibit the same α . In particular, while fine mode aerosols exhibit negative curvature, the presence of sufficient coarse mode aerosols in a bimodal size distribution induces positive curvature due to the efficient extinction of light at longer wavelengths by larger particles. Here, the inlet limited the size range of sampled aerosol to the submicron fraction, such that positive curvature is not expected. Aerosol size distributions were not measured aboard ship during the cruise but as described in Sect. 3.1, previously published work provides sufficient information for a broad characterization of the different ambient aerosol populations prevalent during the three meteorological regimes that occurred during KORUS-OC. This context is used to assess the mapping of SpEx data into (a_1, a_2) space. For clarity, the 60 min mean spectra data are used (Fig. 10).

In addition to the evident separation in α_{ext} across (a_1, a_2) space (Fig. 9 and top left panel of Fig. 10) there is also clear separation as a function of aerosol loading using $\sigma_{\text{ext}}(0.532 \mu\text{m})$ as a proxy for ambient aerosol concentrations (Fig. 10, lower left panel). High concentrations ($\sigma_{\text{ext}}(0.532 \mu\text{m}) > 150 \text{ Mm}^{-1}$) exhibit a relatively small range of a_1 and a_2 values. Generally, these spectra exhibit the greatest curvature (i.e., largest absolute values of a_2 for any given a_1). In contrast, low concentrations ($\sigma_{\text{ext}}(0.532 \mu\text{m}) < 75 \text{ Mm}^{-1}$) span a wide range of values in a_1 and a_2 . As described in Sect. 3.1 there were three distinct meteorological regimes during the cruise (Peterson et al., 2019) that led to different ambient aerosol populations. Hence, the separation in aerosol loading should not be viewed as a function of loading for a uniform aerosol population, but rather as an artifact of the differing size distributions and to a lesser extent, composition.

The (a_1, a_2) map separated according to the defined meteorological regimes reveals strikingly different distributions for the 3 periods (Fig. 10, top right panel). The spectra during the Stagnant period (predominantly submicron aerosols, where $\text{PM}_{2.5} \sim \text{PM}_{10}$ (Jordan et al., 2020a), dominated by locally produced SOA (Kim et al., 2018; Nault et al., 2018; Peterson et al., 2019; Choi et al., 2019;

Formatted: Subscript
Formatted: Subscript

Formatted: Subscript
Formatted: Subscript
Formatted: Font: Symbol

Formatted: Subscript
Formatted: Subscript
Formatted: Subscript
Formatted: Subscript
Formatted: Subscript
Formatted: Subscript
Formatted: Font: 10 pt

Formatted: Subscript
Formatted: Font: 10 pt

Deleted: As λ_{ch} decreases, the mapping rotates counter-clockwise occupying an increasingly narrow band in (a_1, a_2) space (Fig. 9, top right panel).

Formatted: Subscript
Deleted: both to the right and the left of the distribution

Deleted: ,
Deleted: discussed
Deleted: , along with additional inferences made in that section,
Deleted: provide
Deleted: sufficient
Deleted: about the types and sizes of aerosols prevalent in the region during the campaign to enable
Deleted: a broad
Deleted: ment
Deleted: of

525 Jordan et al., 2020a)) produced a remarkably narrow range of a_1 and a_2 values that essentially lie along a single α_{ext} line (~ 1.5) for
the 60 min mean spectra set. In contrast, the spectra during the Blocking period (likely small absorbing aerosols from relatively
fresh ship emissions) exhibit a wide range in a_1 and a_2 values with values of α_{ext} generally > 1.6 . However, α_{ext} values for this
group also span the full range of observed α_{ext} primarily when the absolute value of a_2 was small ($\leq |-0.6|$). The large variability
530 of this group may be due in part to the low extinctions where the sensitivity of α_{ext} to uncertainty in σ_{ext} is greatest. It may also
reflect the heterogeneity of aerosol sources encountered in the marine boundary layer as the ship cruised around the West Sea
during this period.

Finally, the period when aerosol concentrations were highest, Transport/Haze, exhibits the same range in a_1 as the Stagnant
aerosols, but with greater curvature (i.e., larger absolute values of a_2 , Fig. 10, top right panel). During this period the meteorological
535 conditions that transported polluted air masses eastward from China, also created conditions that promoted rapid secondary
inorganic aerosol production locally over the S. Korean peninsula (Peterson et al., 2019; Eck et al., 2020; Jordan et al., 2020a) that
resulted in the growth of fine mode aerosols to larger sizes ($\text{PM}_{2.5} > \text{PM}_{10}$, Eck et al., 2020; Jordan et al., 2020a) than observed
during the Stagnant period. During the first half of the Transport/Haze period the ship was downwind of S. Korea in the East Sea,
while during the second half it was upwind in the West Sea. Splitting the data from this period to reflect the position of the ship
540 (Fig. 10 bottom right panel) shows that the highest concentrations of aerosols were observed downwind of S. Korea and exhibited
the greatest curvature and the lowest α_{ext} . This result indicates larger particle sizes were present downwind than upwind, consistent
with the reported changes in aerosol size distribution due to local production over the Korean peninsula (Eck et al., 2020; Jordan
et al., 2020a). The upwind distribution resembles the narrow Stagnant distribution in (a_1, a_2) space, but shifted to a slightly lower
 α_{ext} .

545 It is interesting to contrast the range in curvature between the three periods. As shown in Fig. 6, α_{ext} decreases as the fit range is
extended to shorter wavelengths. This is due to the curvature evident in the UV range of Fig. 7 which is not adequately captured
by fits to the longer wavelength subranges. In that instance (an individual spectrum from the Stagnant period), $\alpha_{\text{ext}}(0.45\text{-}0.632 \mu\text{m})$
= 3, whereas $\alpha_{\text{ext}}(0.3\text{-}0.7 \mu\text{m}) = 2.04$. The greatest curvature tends to be found for the period with the largest particles observed
550 during the campaign, while for the period when the particles were likely to be smallest, the UV curvature is small or absent leading
to larger α_{ext} values (Fig. 10). In addition, the largest absolute values of a_1 ($\geq |-6|$) found in the individual spectra (Fig. 9) arise
from partial spectra where the longer wavelengths of a measured spectrum are below detection. Spectral fits were limited to only
above detection portions of the measured spectrum. This is why the λ_{ch} for these spectra shift to shorter wavelengths. These
spectra are those for which scattering and extinction were observed to be low, hence, the spectral fit is subject to greater uncertainty.
555 This accounts for the finding that some of the fine fraction Blocking period aerosols, both exhibit curvature as large as the other
two periods, as well as the limited negative curvature ($a_2 \leq |-0.5|$) and in a few cases, slightly positive curvature ($a_2 \geq 0$, Figs. 9 and
10). Note, partial spectra are not suitable for retrievals (i.e., comparable to those from AERONET Level 2 data where at a minimum
above detection values must be available from at least the 0.38, 0.50, and 0.87 μm channels to ensure nonlinearity in the spectrum
is adequately represented). However, partial spectra can be valuable for other analyses such as when combined with absorption
560 coefficients in the calculation of $\omega(\lambda)$ to look for structure in the above detection range for SpEx, particularly in the UV (see Part
2, Jordan et al., 2020b). Hence, partial spectra data are not discarded from further examination.

5 Conclusions

Formatted: Font: Symbol

Formatted: Font: Symbol

Deleted: ¶

565 This work, Part 1 of 2, examined the high temporal resolution data set (IN101, TAP, and SpEx) collected as part of the in situ aerosol measurement suite deployed aboard the *R/V Onnuri* for the KORUS-OC cruise. IN101 scattering (σ_{scat}) and TAP absorption (σ_{abs}) coefficients were measured at three visible wavelengths throughout the cruise, with single scattering albedo (ω) calculated from them. These data were presented to provide an overview of the in situ aerosol measurements throughout the cruise within the context of the prevalent meteorological regimes previously reported for the KORUS-AQ field campaign (Peterson et al., 2019; Jordan et al., 2020a). The cruise took place during 3 distinct meteorological periods where, 1) stagnant conditions 570 fostered local (S. Korean) production of secondary organic aerosol, 2) transport from China coupled with local overcast and humid hazy conditions led to secondary production of inorganic aerosol with rapid growth of fine mode aerosols to larger particle sizes, and 3) a blocking period with limited transport following a frontal passage that dramatically reduced aerosol concentrations. Results presented here suggest the aerosols observed aboard *R/V Onnuri* during this final period were likely relatively fresh small particles from ship emissions into the marine boundary layer. The largest values of σ_{scat} and σ_{abs} were observed when the ship was 575 downwind of the Korean peninsula in the East Sea during the Transport/Haze period. The smallest values of ω were found when the ship was upwind of the peninsula in the West Sea, with low values arising from reductions in scattering rather than increases in absorption.

Extinction coefficients (σ_{ext}) calculated from the 3 visible wavelength σ_{scat} and σ_{abs} data were used to evaluate the performance of 580 SpEx under field conditions that offered a wide range of concentrations, particles sizes, and composition. Excellent agreement was found for all 3 wavelengths with slopes equal to 1.020 ± 0.002 , 0.998 ± 0.003 , and 1.057 ± 0.004 with $r^2 = 0.981$, 0.969 , and 0.942 for the 450, 532, and 632 nm channels, respectively. A lower limit of detection of 10 Mm^{-1} was determined for the individual spectral measurements (twice the standard deviation of the measurement) that can be reduced via standard error of the means when averaging spectra over longer sampling intervals. The broad spectral range (300 - 700 nm) and fine spectral resolution (0.8 nm) 585 provided an opportunity to examine the wavelength dependence of the spectra for a diverse set of in situ ambient aerosols. Nearly all of the measured spectra exhibited curvature in logarithmic space such that 2nd order polynomials provided a better fit to the data than the usual linear fit of a power law representation. With either fit, evidence was presented to highlight the large deviation of an extrapolated value for σ_{ext} beyond the fit wavelength range. This finding highlights the need for measurements that extend well into the UV, thereby limiting the need for extrapolated estimates of σ_{ext} in that part of the spectrum.

590 A comparison to a previous study of spectral curvature based on Mie calculations and remote sensing data from AERONET (Schuster et al., 2006) revealed the wavelength dependence that relates the Angstrom exponent (α) to the 2nd order polynomial coefficients (a_1 and a_2). The characteristic wavelength (λ_{ch}) of any given data set needs to be taken into account when comparing spectral curvature coefficients across data sets. Mapping the fit coefficients shows that any given α representation can be separated 595 along a line in (a_1, a_2) with a slope of $-2\ln(\lambda_{\text{ch}})$ such that spectral curvature can be used to obtain more detailed information about aerosol size distribution. The work of Schuster et al. (2006) was directed to distinguishing different bimodal size distributions on the basis of the presence of coarse fraction aerosols. Here, only fine mode aerosols were sampled, nonetheless, the separation found in (a_1, a_2) space across the KORUS-OC data set suggests that curvature may be used to infer more detailed size distribution information even within the fine mode alone. Size distributions were not measured aboard the *R/V Onnuri*, so such a study will 600 require future ambient measurements to fill this data gap.

Deleted:

In Part 2 (Jordan et al., 2020b), the methodology used for the filter analyses from the KORUS-OC in situ aerosol measurement suite is described with an overview of the results provided. The data from those filters include total aerosol σ_{abs} spectra (300-700 nm) from glass fiber filters placed in the center of an integrating sphere, soluble aerosol absorption coefficient spectra (300-700 nm) from deionized water ($\sigma_{\text{DI-abs}}$) and methanol ($\sigma_{\text{MeOH-abs}}$) extracts of Teflon filters measured with a liquid waveguide capillary cell, water-soluble inorganic ion (WSII) concentrations via ion chromatography, and water-soluble organic compounds (WSOC) that contribute to the aerosol measured using an aerosol mass spectrometer. The combination of filter-based σ_{abs} spectra (300-700 nm) with the SpEx σ_{ext} spectra set, allows for the calculation of spectral ω (300-700 nm) for in situ aerosols. Part 2 includes a similar examination of power law and 2nd order polynomial representations of all 4 of the in situ aerosol hyperspectral data sets obtained during KORUS-OC. It also explores relationships between the optical properties and water-soluble composition information within the meteorological context of KORUS-AQ following the discussion presented here in Part 1.

Data Availability

All data presented here are available under the *R/V Onnuri* Ship tab in the KORUS-AQ archive (DOI: 10.5067/Suborbital/KORUSAQ/DATA01).

Author contribution

CEJ led the experiment, analyzed the data, and wrote the manuscript.
CEJ, BEA, LDZ, CHH, KLT, ELW, RFM, MAS, AJB, CER built elements of the hardware, software, and deployment measurement system; and assisted in the laboratory at NASA LaRC.
CEJ, BEA, AJB, CAC participated in the field work.
RMS, BTL, & MAT deployed with the measurement suite aboard the R/V Onnuri, collected filter samples, and contributed to the manuscript.
GLS, RHM, LDZ, BEA, ECC, MAS, RMS, AJB, & CAC contributed to the data analysis and the manuscript.

Competing interests

The authors declare that they have no conflict of interest.

Acknowledgements

The authors gratefully acknowledge the support of the KORUS-OC and KORUS-AQ science teams, the outstanding support provided by our South Korean partners at the Korean Institute for Ocean Science and Technology (KIOST), and financial support from the NASA/NIA cooperative agreement NNL09AA00A and NASA Grant NNX16AD60G through the Geostationary Coastal and Air Pollution Events (GEO-CAPE) mission pre-formulation studies. The authors particularly thank Anne Thompson for her support throughout this study and Fred Brechtel and Vanderlei Martins for helpful discussions

References

- Al-Saadi, J., Carmichael, G., Crawford, J., Emmons, L., Kim, S., Song, C.-K., Chang, L.-S., Lee, G., Kim, J., and Park, R.: NASA Contributions to KORUS-AQ: An International Cooperative Air Quality Field Study in Korea, available on-line at
635 https://espo.nasa.gov/home/korus-aq/content/KORUS-AQ_Science_Overview_0, 32 pages, 2015.
- Anderson, T. L., and Ogren, J. A.: Determining aerosol radiative properties using the TSI 3563 integrating nephelometer, *Aerosol Sci. & Technol.*, 29:1, 57-69, doi: 10.1080/02786829808965551, 1998.
- 640 Ångström, A.: On the atmospheric transmission of sun radiation and on dust in the air (1929), in *Selected papers on scattering in the atmosphere*, SPIE Milestone Series, vol. 11, edited by C. Bohren, pp. 156–166, SPIE, 1989.
- Bluvshstein, N., Flores, J. M., Segev, L., and Rudich, Y.: A new approach for retrieving the UV-Vis optical properties of ambient aerosols, *Atmos. Meas. Tech.*, 9(8), 3477–3490, doi:10.5194/amt-9-3477-2016, 2016.
- 645 Bluvshstein, N., Lin, P., Flores, J. M., Segev, L., Mazar, Y., Tas, E., Snider, G., Weagle, C., Brown, S. S., Laskin, A., Rudich, Y.: Broadband optical properties of biomass-burning aerosol and identification of brown carbon chromophores, *J. Geophys. Res.-Atmos.*, 122 (10), 5441–5456, doi:10.1002/2016JD026230, 2017.
- 650 Chartier, R. T. and Greenslade, M. E.: Initial investigation of the wavelength dependence of optical properties measured with a new multi-pass Aerosol Extinction Differential Optical Absorption Spectrometer (AE-DOAS), *Atmos. Meas. Tech.*, 5, 709–721, doi:10.5194/amt-5-709-2012, 2012.
- Choi, J., Park, R. J., Lee, H. M., Lee, S., Jo, D. S., Jeong, J. I., Henze, D. K., Woo, J. H., Ban, S. J., Lee, M. D., Lim, C. S., Park, M. K., Shin, H. J., Cho, S., Peterson, D., and Song, C. K.: Impacts of local vs. trans-boundary emissions from different sectors on PM_{2.5} exposure in South Korea during the KORUS-AQ campaign, *Atmos. Environ.*, 203, 196–205, <https://doi.org/10.1016/j.atmosenv.2019.02.008>, 2019.
- 655 Crawford, J. H., Ahn, J.-Y., Al-Saadi, J., Chang, L., Emmons, L. K., Kim, J., Lee, G., Park, J.-H., Park, R., Woo, J. H., Lefer, B. L., Lee, M., Lee, T., Kim, S., Min, K.-E., Yum, S. S., Szykman, J. J., Jordan, C. E., Simpson, I. J., Fried, A., Cho, S., and Kim, Y. P.: The Korea-United States Air Quality (KORUS-AQ) field study, *submitted to Elem. Sci. Anth.*, October 2020.
- Eck, T. F., Holben, B. N., Reid, J. S., Dubovik, O., Smirnov, A., O'Neill, N. T., Slutsker, I., and Kinne, S.: Wavelength dependence of the optical depth of biomass burning, urban, and desert dust aerosols, *J. Geophys. Res.*, 104:D24, 31,333–31,349, 1999.
- 665 Eck, T. F., Holben, B. N., Dubovik, O., Smirnov, A., Slutsker, I., Lobert, J. M., and Ramanathan, V.: Column-integrated aerosol optical properties over the Maldives during the northeast monsoon for 1998–2000, *J. Geophys. Res.*, 106:D22, 28,555–28,566, 2001a.
- 670 Eck, T. F., Holben, B. N., Ward, D. E., Dubovik, O., Reid, J. S., Smirnov, A., Mukelabai, M. M., Hsu, N. C., O'Neill, N. T., and Slutsker, I.: Characterization of the optical properties of biomass burning aerosols in Zambia during the 1997 ZIBBEE field campaign, *J. Geophys. Res.*, 106:D4, 3425–3448, 2001b.

Formatted: Font: Times New Roman, 10 pt

Formatted: Space Before: 0 pt, After: 0 pt, Line spacing: 1.5 lines

Formatted: Font: 10 pt

- Eck, T. F., Holben, B. N., Ward, D. E., Mukelabai, M. M., Dubovik, O., Smirnov, A., Schafer, J. S., Hsu, N. C., Piketh, S. J.,
675 Queface, A., Le Roux, J., Swap, R. J., and Slutsker, I.: Variability of biomass burning aerosol optical characteristics in southern
Africa during the SAFARI 2000 dry season campaign and a comparison of single scattering albedo estimates from radiometric
measurements, *J. Geophys. Res.*, 108:D13, 8477, doi:10.1029/ 2002JD002321, 2003a.
- Eck, T. F., Holben, B. N., Ward, D. E., Mukelabai, M. M., Dubovik, O., Smirnov, A., Schafer, J. S., Hsu, N. C., Piketh, S. J.,
680 Queface, A., Le Roux, J., Swap, R. J., and Slutsker, I.: Correction to “Variability of biomass burning aerosol optical characteristics
in southern Africa during the SAFARI 2000 dry season campaign and a comparison of single scattering albedo estimates from
radiometric measurements” by T. F. Eck et al., *J. Geophys. Res.*, 108:D13, 8500, doi:10.1029/2003JD001606, 2003b.
- Eck, T. F., Holben, B. N., Kim, J., Beyersdorf, A. J., Choi, M., Lee, S., Koo, J. H., Giles, D. M., Schafer, J. S., Sinyuk, A., Peterson,
685 D. A., Reid, J. S., Arola, A., Slutsker, I., Smirnov, A., Sorokin, M., Kraft, J., Crawford, J. H., Anderson, B. E., Thornhill, K. L.,
Diskin, G., Kim, S. W., and Park, S.: Influence of cloud, fog, and high relative humidity during pollution transport events in South
Korea: aerosol properties and PM_{2.5} variability, *Atmos. Environ.*, 232, 117530, <https://doi.org/10.1016/j.atmosenv.2020.117530>,
2020.
- Fu, G., Hasekamp, O., Rietjens, J., Smit, M., Di Noia, A., Cairns, B., Wasilewski, A., Diner, D., Seidel, F., Xu, F., Knobelspiesse,
690 K., Gao, M., da Silva, A., Burton, S., Hostetler, C., Hair, J., and Ferrare, R.: Aerosol retrievals from different polarimeters during
the ACEPOL campaign using a common retrieval algorithm, *Atmos. Meas. Tech.*, 13, 553–573, <https://doi.org/10.5194/amt-13-553-2020>, 2020.
- Giles, D. M., Sinyuk, A., Sorokin, M. G., Schafer, J. S., Smirnov, A., Slutsker, I., Eck, T. F., Holben, B. N., Lewis, J. R., Campbell,
695 J. R., Welton, E. J., Korkin, S. V., and Lyapustin, A. I.: Advancements in the Aerosol Robotic Network (AERONET) Version 3
database – automated near-real-time quality control algorithm with improved cloud screening for Sun photometer aerosol optical
depth (AOD) measurements, *Atmos. Meas. Tech.*, 12, 169–209, <https://doi.org/10.5194/amt-12-169-2019>, 2019.
- Hasekamp, O. P., Fu, G., Rusli, S. P., Wu, L., Di Noia, A., aan de Brugh, J., Landgraf, J., Smit, J. M., Rietjens, J., van Amerongen,
700 A.: Aerosol measurements by SPEXone on the NASA PACE mission: expected retrieval capabilities, *J. Quant. Spec. & Rad. Trans.*,
227, 170-184, <https://doi.org/10.1016/j.jqsrt.2019.02.006>, 2019.
- He, Q., Bluvshstein, N., Segev, L., Meidan, D., Flores, J. M., Brown, S. S., Brune, W., and Rudich, Y.: Evolution of the Complex
705 Refractive Index of Secondary Organic Aerosols during Atmospheric Aging, *Environ. Sci. Technol.*, 52, 3456–3465, DOI:
10.1021/acs.est.7b05742, 2018.
- Jordan, C. E., Anderson, B. E., Beyersdorf, A. J., Corr, C. A., Dibb, J. E., Greenslade, M. E., Martin, R. F., Moore, R. H., Scheuer,
E., Shook, M. A., Thornhill, K. L., Troop, D., Winstead, E. L., and Ziemba, L. D.: Spectral aerosol extinction (SpEx): a new
710 instrument for in situ ambient aerosol extinction measurements across the UV/visible wavelength range, *Atmos. Meas. Tech.*, 8,
4755–4771, doi:10.5194/amt-8-4755-2015, 2015.

- Jordan, C. E., Crawford, J. H., Beyersdorf, A. J., Eck, T. F., Halliday, H. S., Nault, B. A., Chang, L.-S., Park, J., Park, R., Lee, G., Kim, H., Ahn, J.-Y., Cho, S., Shin, H. J., Lee, J. H., Jung, J., Kim, D.-S., Lee, M., Lee, T., Whitehill, A., Szykman, J., Schueneman, M. K., Campuzano-Jost, P., Jimenez, J. L., DiGangi, J. P., Diskin, G. S., Anderson, B. E., Moore, R. H., Ziemba, L. D., Fenn, M. A., Hair, J. W., Kuehn, R. E., Holz, R. E., Chen, G., Travis, K., Shook, M., Peterson, D. A., Lamb, K. D., and Schwarz, J. P.: Investigation of factors controlling PM_{2.5} variability across the South Korean Peninsula during KORUS-AQ, *Elem. Sci. Anth.*, 8, 28, doi:10.1525/elementa.424, 2020a.
- 715
- Jordan, C. E., Stauffer, R. M., Lamb, B. T., Novak, M. Mannino, A., Crosbie, E., Schuster, G. L., Moore, R., Hudgins, C., Thornhill, K. L., Winstead, E. L., Anderson, B. E., Martin, R. F., Shook, M. A., Ziemba, L. D., Beyersdorf, A. J., Robinson, C., Corr, C. A., and Tzortziou, M.: New in situ aerosol hyperspectral optical measurements over 300–700 nm, Part 2: Extinction, total absorption, water- and methanol-soluble absorption observed during the KORUS-OC cruise, *in review Atmos. Meas. Tech.*, amt-2020-318, 2020b.
- 720
- Kaku, K. C., Reid, J. S., O'Neill, N. T., Quinn, P. K., Coffman, D. J., and Eck, T. F.: Verification and application of the extended spectral deconvolution algorithm (SDA+) methodology to estimate aerosol fine and coarse mode extinction coefficients in the marine boundary layer, *Atmos. Meas. Tech.*, 7, 3399–3412, <https://doi.org/10.5194/amt-7-3399-2014>, 2014.
- 725
- Kaskaoutis, D. G., Kalapureddy, M. C. R., Moorthy, K. K., Devara, P. C. S., Nastos, P. T., Kosmopoulos, P. G., and Kambezidis, H. D.: Heterogeneity in pre-monsoon aerosol types over the Arabian Sea deduced from ship-borne measurements of spectral AODs, *Atmos. Chem. Phys.*, 10, 4893–4908, doi:10.5194/acp-10-4893-2010, 2010.
- 730
- Kaskaoutis, D. G., Kharol, S. K., Sinha, P. R., Singh, R. P., Kambezidis, H. D., Sharma, A. R., and Badarinath, K. V. S.: Extremely large anthropogenic-aerosol contribution to total aerosol load over the Bay of Bengal during winter season, *Atmos. Chem. Phys.*, 11, 7097–7117, doi:10.5194/acp-11-7097-2011, 2011.
- 735
- Kaufman, Y. J.: Aerosol optical thickness and atmospheric path radiance, *J. Geophys. Res.*, 98:D2, 2677–2692, 1993.
- 740
- Kim, H., Zhang, Q., and Heo, J.: Influence of intense secondary aerosol formation and long-range transport on aerosol chemistry and properties in the Seoul Metropolitan Area during spring time: results from KORUS-AQ, *Atmos. Chem. Phys.*, 18, 7149–7168, <https://doi.org/10.5194/acp-18-7149-2018>, 2018.
- 745
- King, M. D., and Byrne, D. M.: A method for inferring total ozone content from the spectral variation of total optical depth obtained with a solar radiometer, *J. Atmos. Sci.*, 33, 2242–2251, 1976.
- King, M. D., Byrne, D. M., Herman, B. M., and Reagan, J. A.: Aerosol size distributions obtained by inversion of spectral optical depth measurements, *J. Atmos. Sci.*, 35, 2153–2167, 1978.
- 750
- LeBlanc, S. E., Redemann, J., Flynn, C., Pistone, K., Kacenelenbogen, M., Segal-Rosenheimer, M., Shinozuka, Y., Dunagan, S., Dahlgren, R. P., Meyer, K., Podolske, J., Howell, S. G., Freitag, S., Small-Griswold, J., Holben, B., Diamond, M., Wood, R.,

Deleted: submitted to Atmos. Chem. Phys.

Formatted: Font: Times New Roman, 10 pt

Formatted: Line spacing: 1.5 lines

Formatted: Font: 10 pt

- Formenti, P., Piketh, S., Maggs-Kölling, G., Gerber, M., and Namwoonde, A.: Above-cloud aerosol optical depth from airborne observations in the southeast Atlantic, *Atmos. Chem. Phys.*, 20, 1565–1590, <https://doi.org/10.5194/acp-20-1565-2020>, 2020.
- 755 Moosmüller, H., and Chakrabarty, R. K.: Technical Note: Simple analytical relationships between Ångström coefficients of aerosol extinction, scattering, absorption, and single scattering albedo, *Atmos. Chem. Phys.*, 11, 10677–10680, doi:10.5194/acp-11-10677-2011, 2011.
- 760 Nault, B. A., Campuzano-Jost, P., Day, D. A., Schroder, J. C., Anderson, B., Beyersdorf, A. J., Blake, D. R., Brune, W. H., Choi, Y., Corr, C. A., de Gouw, J. A., Dibb, J., DiGangi, J. P., Diskin, G. S., Fried, A., Huey, L. G., Kim, M. J., Knote, C. J., Lamb, K. D., Lee, T., Park, T., Pusede, S. E., Scheuer, E., Thornhill, K. L., Woo, J. H., and Jimenez, J. L.: Secondary organic aerosol production from local emissions dominates the organic aerosol budget over Seoul, South Korea, during KORUS-AQ, *Atmos. Chem. Phys.*, 18, 17,769–17,800, <https://doi.org/10.5194/acp-18-17769-2018>, 2018.
- 765 O'Neill, N. T., Dubovik, O., and Eck, T. F.: Modified Ångström exponent for the characterization of submicrometer aerosols, *Appl. Opt.*, 40:15, 2368 – 2375, 2001.
- 770 O'Neill, N. T., Eck, T. F., Smirnov, A., Holben, B. N., and Thulasiraman S.: Spectral discrimination of coarse and fine mode optical depth, *J. Geophys. Res.-Atmos.*, 108, 4559, doi:10.1029/2002JD002975, 2003.
- O'Neill, N. T., Eck, T. F., Reid, J. S., Smirnov, A., and Pancrati, O.: Coarse mode optical information retrievable using ultraviolet to short-wave infrared Sun photometry: Application to United Arab Emirates Unified Aerosol Experiment data, *J. Geophys. Res.- Atmos.*, 113, D05212, doi:10.1029/2007JD009052, 2008.
- 775 Ogren, J. A., Wendell, J., Andrews, E., and Sheridan, P. J.: Continuous light absorption photometer for long-term studies, *Atmos. Meas. Tech.*, 10, 4805-4818, <https://doi.org/10.5194/amt-10-4805-2017>, 2017.
- Peterson, D. A., Hyer, E. J., Han, S.-O., Crawford, J. H., Park, R. J., Holz, R., Kuehn, R. E., Eloranta, E., Knote, C., Jordan, C. E., and Lefer, B. L.: Meteorology influencing springtime air quality, pollution transport, and visibility in Korea, *Elem. Sci. Anth.*, 7, 57, doi:<https://doi.org/10.1525/elementa.395>, 2019.
- 780 Rao, B. M., and Niranjan, K.: Optical properties of the South Asian winter haze at a tropical coastal site in India, *Atmos. Environ.*, 54, 449-455, doi:10.1016/j.atmosenv.2012.02.016, 2012.
- 785 Reid, J. S., Eck, T. F., Christopher, S. A., Hobbs, P. V., and Holben, B.: Use of the Ångström exponent to estimate the variability of optical and physical properties of aging smoke particles in Brazil, *J. Geophys. Res.*, 104:D22, 27,473 – 27,489, 1999.
- 790 Remer, L. A., Davis, A. B., Mattoo, S., Levy, R. C., Kalashnikova, O. V., Coddington, O., Chowdhary, J., Knobelspiesse, K., Xu, X., Ahmad, Z., Boss, E., Cairns, B., Dierssen, H. M., Diner, D. J., Franz, B., Frouin, R., Gao, B.-C., Ibrahim, A., Martins, J. V., Omar, A. H., Torres, O., Xu, F., and Zhai, P.-W.: Retrieving Aerosol Characteristics From the PACE Mission, Part 1: Ocean Color Instrument, *Front. Earth Sci.*, 7:152. doi:10.3389/feart.2019.00152, 2019a.

Formatted: Font: Times New Roman, 10 pt

Formatted: Line spacing: 1.5 lines

Formatted: Font: 10 pt

Formatted: Space Before: 0 pt, After: 0 pt, Line spacing: 1.5 lines

Formatted: Font: Times New Roman, 10 pt

Formatted: Font: 10 pt

Formatted: Space Before: 0 pt, After: 0 pt, Line spacing: 1.5 lines

Remer, L. A., Knobelspiesse, K., Zhai, P.-W., Xu, F., Kalashnikova, O. V., Chowdhary, J., Hasekamp, O., Dubovik, O., Wu, L., Ahmad, Z., Boss, E., Cairns, B., Coddington, O., Davis, A. B., Dierssen, H. M., Diner, D. J., Franz, B., Frouin, R., Gao, B.-C., Ibrahim, A., Levy, R. C., Martins, J. V., Omar, A. H., and Torres, O. Retrieving Aerosol Characteristics From the PACE Mission, Part 2: Multi-Angle and Polarimetry, *Front. Environ. Sci.*, 7:94. doi:10.3389/fenvs.2019.00094, 2019b.

Schuster, G. L., Dubovik, O., and Holben, B. N.: Angstrom exponent and bimodal aerosol size distributions, *J. Geophys. Res.*, 111, D07207, doi:10.1029/2005JD006328, 2006.

Smit, J. M., Rietjens, J. H. H., van Harten, G., Noia, A. D., Laauwen, W., Rheingans, B. E., Diner, D. J., Cairns, B., Wasilewski, A., Knobelspiesse, K. D., Ferrare, R., and Hasekamp, O. P.: SPEX airborne spectropolarimeter calibration and performance, *Appl. Optics*, 58, 5695–5719, <https://doi.org/10.1364/AO.58.005695>, 2019.

Thompson, A. M., Stauffer, R. M., Boyle, T. P., Kollonige, D. E., Miyazaki, K., Tzortziou, M., Herman, J. R., Abuhassan, N., Jordan, C. E., and Lamb, B. T.: Comparison of near surface NO₂ pollution with Pandora total column NO₂ during the Korea-United States Ocean Color (KORUS OC) Campaign, *J. Geophys. Res.: Atmos.*, 124, 13,560–13,575, <https://doi.org/10.1029/2019JD030765>, 2019.

Tzortziou, M., Parker, O., Lamb, B., Herman, J., Lamsal, L., Stauffer, R., and Abuhassan, N.: Atmospheric trace gas (NO₂ and O₃) variability in Korean coastal waters, implications for remote sensing of coastal ocean color dynamics, *Remote Sens.*, 10(10), 1587; doi:10.3390/rs10101587, 2018.

US-Korean Steering Group: Risk reduction measurements for GEO-CAPE: A US-Korea joint field campaign (US-Korea JFC) in the East Sea and Yellow Sea, available on-line at https://geo-cape.larc.nasa.gov/pdf/KORUS_OC_WhitePaper_2016_Field_20150205_final.pdf, 18 pages, 2015.

Washenfelder, R. A., Flores, J. M., Brock, C. A., Brown, S. S., and Rudich, Y.: Broadband measurements of aerosol extinction in the ultraviolet spectral region, *Atmos. Meas. Tech.*, 6, 861–877, doi:10.5194/amt-6-861-2013, 2013.

Washenfelder, R. A., Attwood, A. R., Brock, C. A., Guo, H., Xu, L., Weber, R. J., Ng, N. L., Allen, H. M., Ayres, B. R., Baumann, K., Cohen, R. C., Draper, D. C., Duffey, K. C., Edger-ton, E., Fry, J. L., Hu, W. W., Jimenez, J. L., Palm, B. B., Romer, P., Stone, E. A., Wooldridge, P. J., and Brown, S. S.: Biomass burning dominates brown carbon absorption in the rural southeastern United States, *Geophys. Res. Lett.*, 42, 653–664, doi:10.1002/2014GL062444, 2015.

Werdell, P. J., Behrenfeld, M. J., Bontempi, P. S., Boss, E., Cairns, B., Davis, G. T., Franz, B. A., Gliese, U. B., Gorman, E. T., Hasekamp, O., Knobelspiesse, K. D., Mannino, A., Martins, J. V., McClain, C. R., Meister, G., and Remer, L. A.: The Plankton, Aerosol, Cloud, ocean Ecosystem mission status, science, advances, *BAMS*, 1775–1794, doi:10.1175/BAMS-D-18-0056.1, 2019.

White, J. U.: Long optical paths of large aperture, *J. Opt. Soc. Am.*, 32, 285–288, 1942.

Deleted: ¶

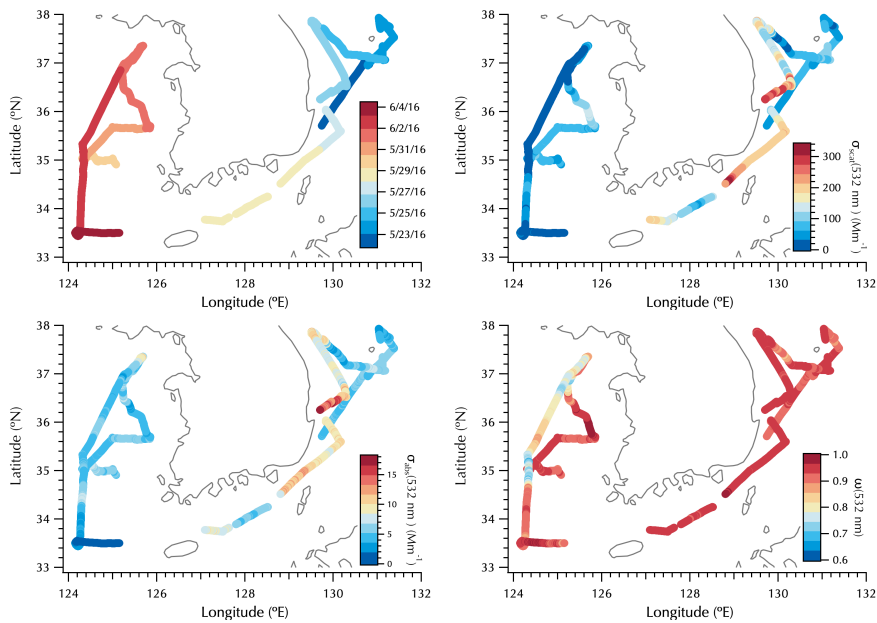
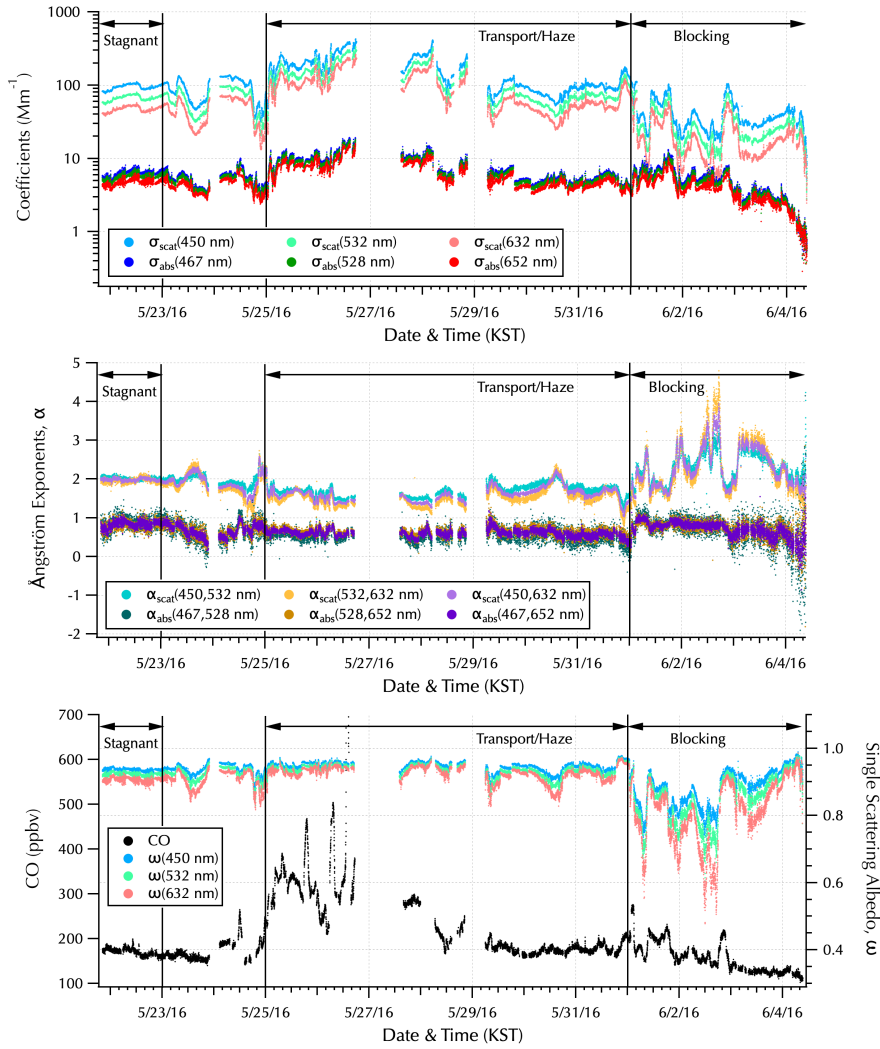


Figure 1: Cruise maps of date and time (KST, top left) with 532 nm σ_{scat} (Mm^{-1} , top right), σ_{abs} (Mm^{-1} , bottom left) and ω (bottom right).



840

Figure 2: Top: σ_{scat} (light shades) and σ_{abs} (dark shades) averaged to 1 minute intervals during the cruise (both in units of Mm^{-1}). Middle: α_{scat} (light shades) and α_{abs} (dark shades), unitless, calculated from the wavelength pairs of the coefficients in the top panel. Bottom: ω (right axis), unitless, along with 1 minute averaged CO concentrations (ppbv). Note, the peak CO value cut off in the figure reached 1000 ppbv.

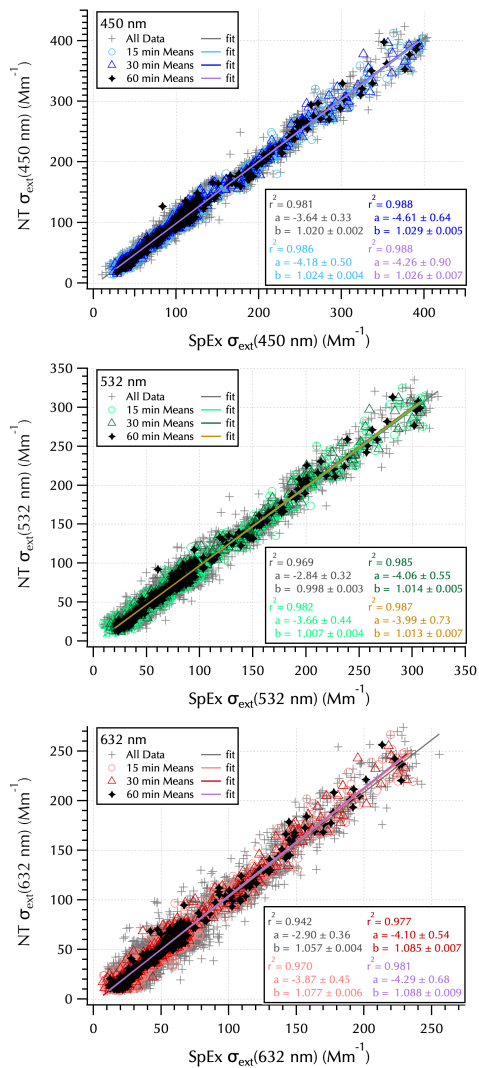
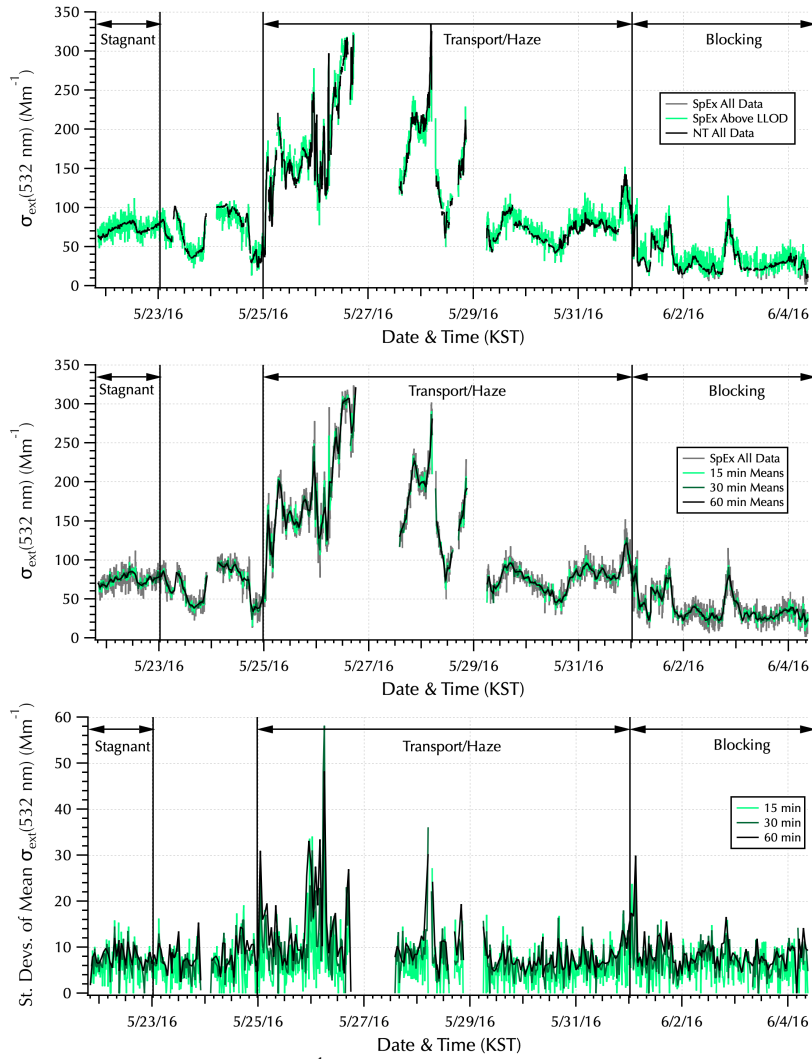
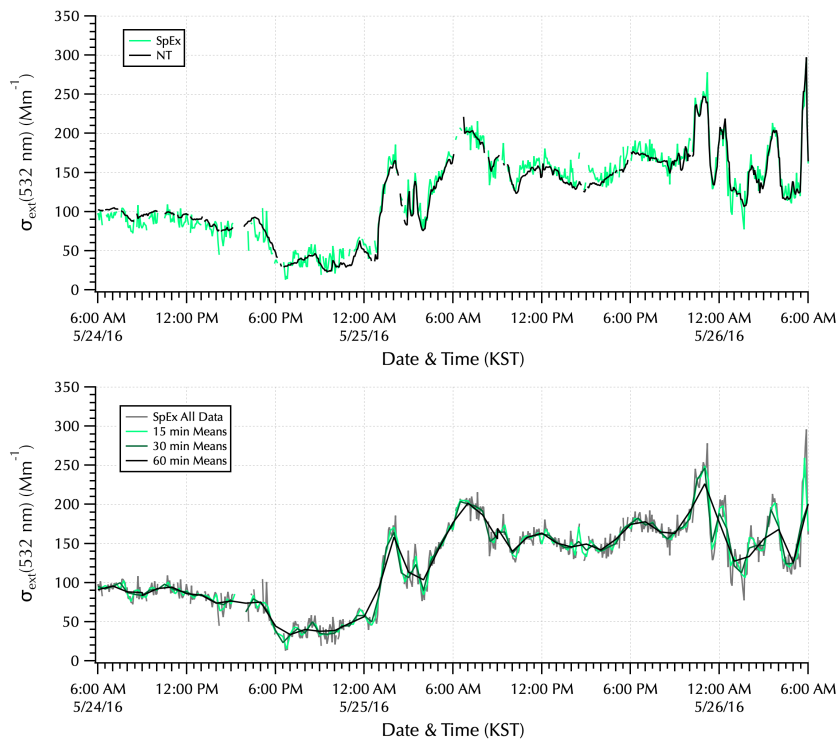


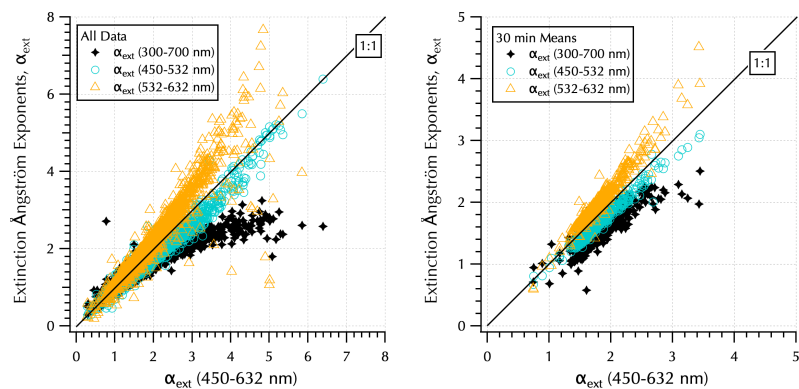
Figure 3: NT vs. SpEx σ_{ext} (450 nm, top; 532 nm, middle; 632 nm bottom) All data points (gray pluses) are shown with 15 min (light colored circles), 30 min (dark colored triangles), and 60 min (black symbols) means. Fit lines, coefficients, and r^2 values are color-coordinated with the symbols, except for the black markers where the fit lines used a light color for visibility. Above LLOD points only.



855 **Figure 4:** Time series of 532 nm σ_{ext} (Mm^{-1}) throughout the cruise. Top panel: SpEx (all data, gray; above LLOD, green; these curves are coincident until June 2nd when the lowest values are below detection and hence, appear gray) with NT σ_{ext} (black). Middle panel: SpEx (all data, gray) with 15 min (light green), 30 min (dark green), and 60 min (black) means. Bottom panel: SpEx standard deviations of the 15 min (light green), 30 min (dark green), and 60 min (black) means. Meteorological periods shown as in Fig. 2.



860 **Figure 5:** Two day highlight of the top two panels of Fig. 4. Top panel: $\sigma_{\text{ext}}(532 \text{ nm})$ from SpEx (green) shown with NT (black). Bottom panel: $\sigma_{\text{ext}}(532 \text{ nm})$ from SpEx (all data, gray) with 15 min (light green), 30 min (dark green), and 60 min (black) means.



865 **Figure 6: α_{ext} determined over 3 different wavelength ranges (300-700 nm, black diamonds, 450-532 nm, teal circles, and 532-632 nm, gold triangles) compared to that found over the 450-632 nm range (x-axis). All data (left panel) and 30 min means (right).**

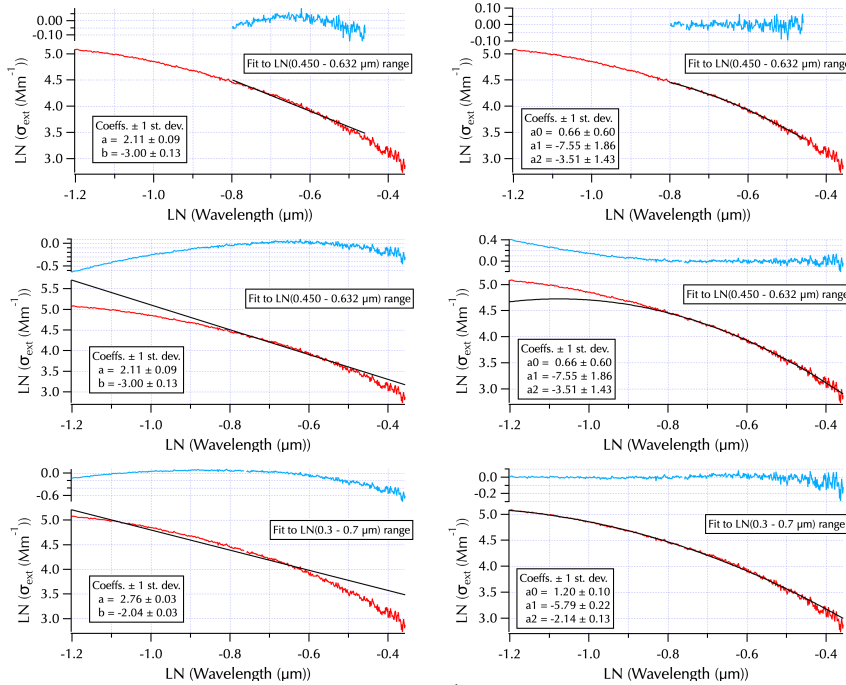


Figure 7. Example of wavelength dependence of $\text{LN}(\sigma_{\text{ext}} \text{ (Mm}^{-1}\text{)})$ spectra (red curves) as a function of $\text{LN}(\text{wavelength } \mu\text{m})$. Linear ($y = a + b(x)$, left panels; here the intercept $a = \text{LN}(B)$, the value of $\text{LN}(\sigma_{\text{ext}})$ at $1 \mu\text{m}$ where $\text{LN}(1 \mu\text{m}) = 0$, and the slope $b = -\alpha$) and 2nd order polynomial ($y = a_0 + a_1(x) + a_2(x^2)$, right panels) fits (black curves) are shown with the fit residuals ($= \text{LN}(\sigma_{\text{ext}} \text{ (Mm}^{-1}\text{)}) - \text{fit}$, blue curves). Residuals randomly distributed around zero indicate a good fit by the mathematical function used to fit the data, trends in residuals suggest another function may provide a better fit. Top and bottom panels show fits to a subrange ($\text{LN}(0.450 - 0.632 \mu\text{m})$) and full range ($\text{LN}(0.3 - 0.7 \mu\text{m})$) of the measured spectrum, respectively. Middle panels show the extrapolation of the fit in the top panels over the full measured wavelength range. The x-axis labels of -1.2, -1.0, -0.8, -0.6 and -0.4 for $\text{LN}(\lambda \text{ (}\mu\text{m)})$ equal 0.301, 0.368, 0.449, 0.549, 0.670, and 0.698 μm wavelengths, respectively.

Formatted: Font: Symbol

Formatted: Font: Symbol

Formatted: Font: Symbol

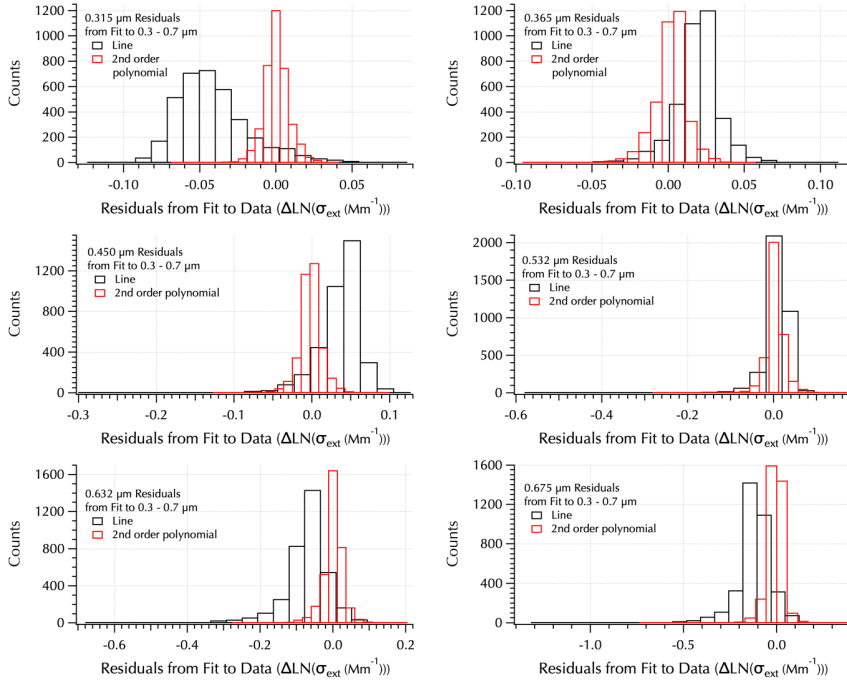


Figure 8: Comparison of residuals (the difference between the data and mathematical function fit to that data) from a line fit (black) and 2nd order polynomial fit (red) to the measured $\text{LN}(\sigma_{\text{ext}}(\text{Mm}^{-1}))$ spectra over the 0.3 - 0.7 μm range for 6 wavelengths: 0.315 (top left), 0.365 (top right), 0.45 (middle left), 0.532 (middle right), 0.632 (bottom left), and 0.675 μm (bottom right).

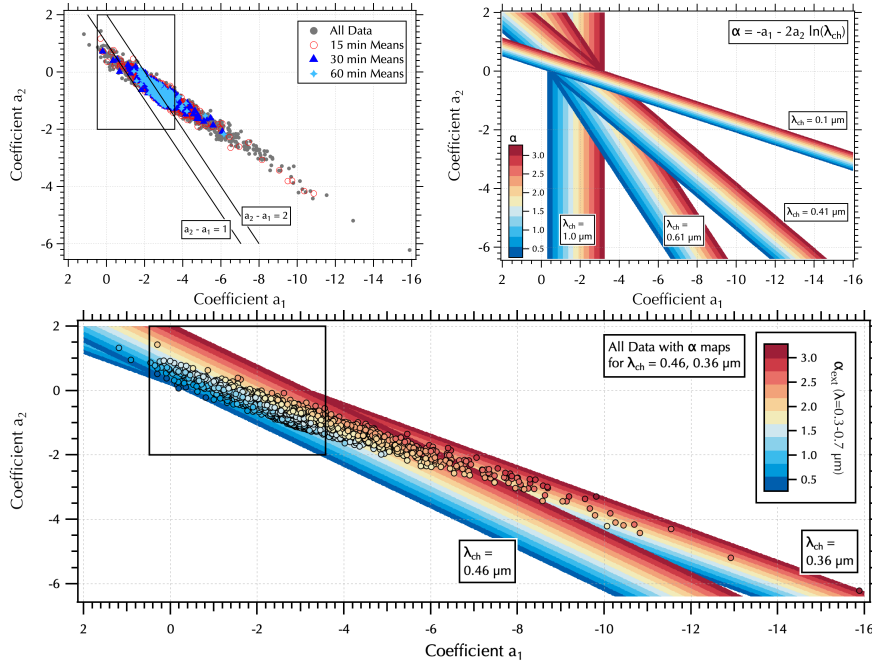


Figure 9: Top left: coefficients a_2 versus a_1 from 2nd order polynomial fits to the full wavelength range (0.3 - 0.7 μm) of the individual (All Data, gray filled circles) and mean (15 min, red open circles, 30 min, dark blue triangles, and 60 min, light blue diamonds, average) spectra. **The black box shows the limits of the Schuster et al. [2006] Fig. 6 plot, black lines show approximate equivalents to $\alpha_{\text{ext}} = 1$ and 2 from that work.** Top right: α mapped into (a_1, a_2) space as a function of the characteristic wavelength (λ_{ch}) of the measured spectral range. Bottom: α_{ext} calculated from the full spectral range of SpEx (colored dots) overlaid on α maps that cover the range of λ_{ch} values calculated from the data set. **The black box is the same as the one in the top left panel.**

Deleted: B

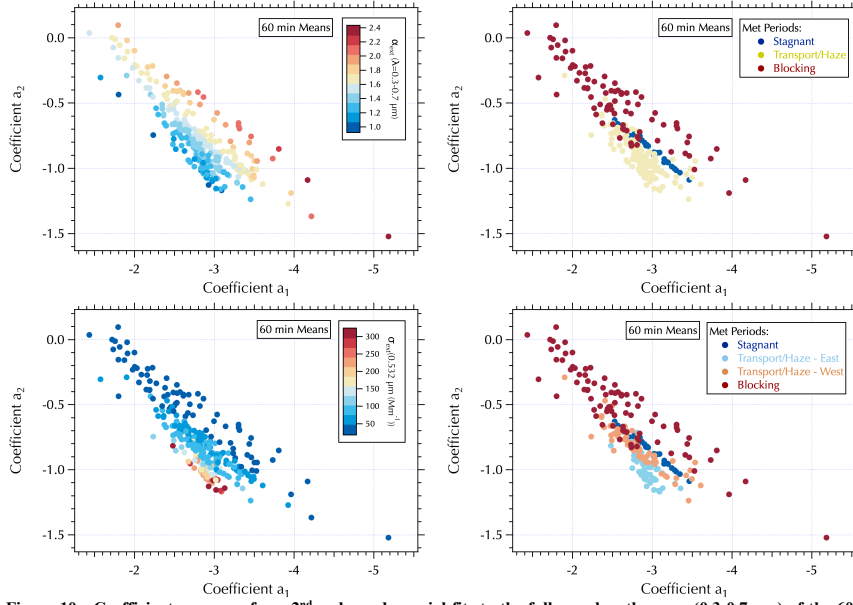


Figure 10: Coefficients a_2 vs. a_1 from 2nd order polynomial fits to the full wavelength range (0.3-0.7 μm) of the 60 min mean spectra colored by $\alpha_{\text{ext}} (\lambda=0.3-0.7 \mu\text{m})$, top left, $\sigma_{\text{ext}} (0.532 \mu\text{m})$, bottom left, and the defined meteorological periods described in Peterson et al. [2019], top right (i.e., excluding the interval when the meteorological regime was in transition, May 23rd and 24th, and hence, undefined). The bottom right panel is the same as the top right, but with the Transport/Haze samples split between those measured to the east (May 25th-27th) and west (May 29th-31st) of the peninsula, excluding those samples collected in transit between the two.

[▲]Supplemental Information for

Formatted: Font: Italic

Formatted: Font: Bold, Italic

New In Situ Aerosol Hyperspectral Optical Measurements over 300-700 nm, Part 1: Spectral Aerosol Extinction (SpEx) Instrument Field Validation during the KORUS-OC cruise

Carolyn E. Jordan^{1,2}, Ryan M. Stauffer³, Brian T. Lamb⁴, Charles H. Hudgins², Kenneth L. Thornhill^{2,5}, Gregory L. Schuster², Richard H. Moore², Ewan C. Crosbie^{2,5}, Edward L. Winstead^{2,5}, Bruce E. Anderson², Robert F. Martin², Michael A. Shook², Luke D. Ziemba², Andreas J. Beyersdorf^{2,6}, Claire E. Robinson^{2,5}, Chelsea A. Cori^{2,7} and Maria A. Tzortziou^{3,4}

¹National Institute of Aerospace, Hampton, Virginia, United States of America

²NASA Langley Research Center, Hampton, Virginia, United States of America

³NASA Goddard Space Flight Center, Greenbelt, Maryland, United States of America

⁴City University of New York, New York, New York, United States of America

⁵Science Systems and Applications Inc., Hampton, Virginia, United States of America

⁶California State University, San Bernardino, California, United States of America

⁷Springfield College, Springfield, Massachusetts, United States of America

Correspondence to: C. E. Jordan (Carolyn.Jordan@nasa.gov)



Figure S1. *R/V Onnuri* (top photo); instruments housed in custom-built box sited along the starboard rail above the bridge (long box, left half of bottom left photo, with tall curved sampling mast just to its right); pumps housed in a separate box located a few meters away along the stern rail (bottom right photo).

Formatted: Font: 10 pt

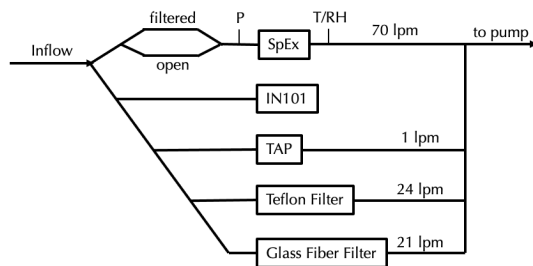


Figure S2. Schematic of the flow through the in situ aerosol instrument suite deployed aboard the *R/V Onnuri*. Note that the IN101 has an internal fan that controls its flow, hence, it is not connected to the pump as are the rest of the instruments.

Formatted: Font: Italic

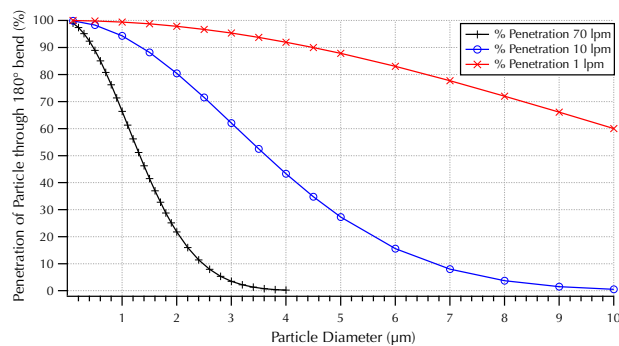


Figure S3. Illustration of the relationship between flow rate and size cut of the sampled aerosol particles based on theoretical calculations pertinent to the system deployed aboard the *R/V Onnuri*.

Deleted: 2

Formatted: Font: 10 pt

Formatted: Font: Italic

Deleted: .

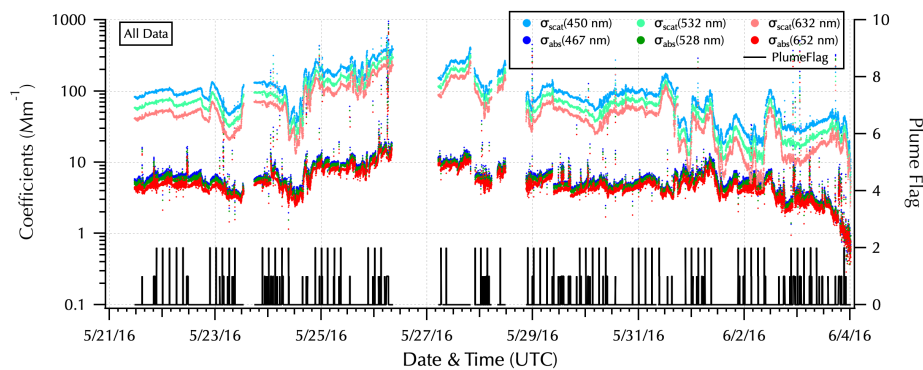


Figure S4. All measured scattering coefficients (σ_{scat} , light shades) and absorption coefficients (σ_{abs} , dark shades) averaged to 1 minute intervals during the cruise (left axis, units of Mm^{-1}), along with plume flags (right axis, = 0 ambient data, = 1 ship exhaust interception, and = 2 filter changes).

Formatted: Font: 10 pt

Deleted: 3

Deleted: ¶

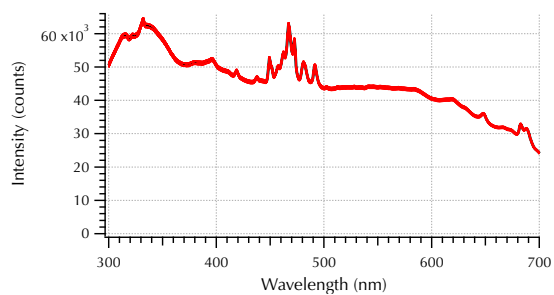


Figure S5. Example of a one hour set of intensity spectra that illustrate the two wavelengths (332 nm and 467 nm) that sometimes saturated due to drift in the lamp intensity. 30 individual spectra measured at 2 min intervals over the course of one hour are shown. Typically (as is the case here) there is little discernible difference in intensity between sample and reference spectra over the full range of counts in the 16 bit spectrometer (0-65,536 counts).

Formatted: Font: 10 pt

Deleted: 4

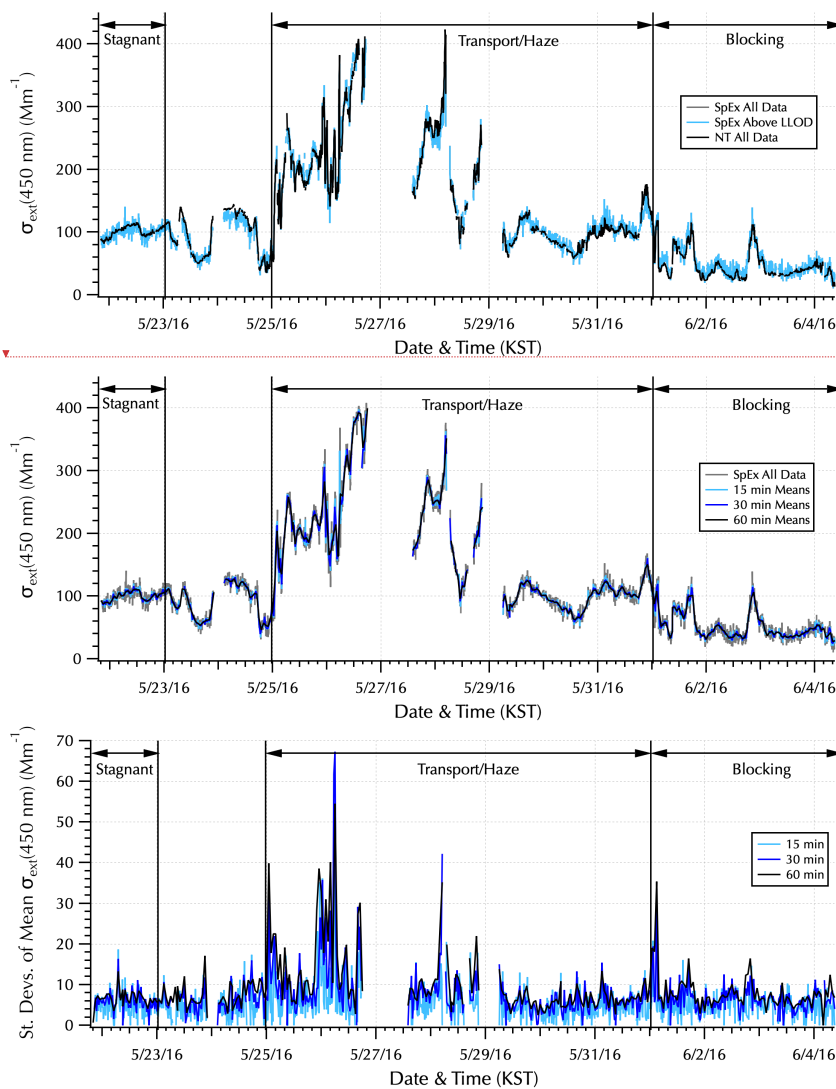


Figure S6. Time series of 450 nm σ_{ext} (Mm^{-1}) throughout the cruise. Top panel: SpEx (all data, gray; above LLOD, blue; these curves are entirely coincident as there were no below detection values at this wavelength) with NT σ_{ext} (black). Middle panel: SpEx (all data, gray) with 15 min (light blue), 30 min (dark blue), and 60 min (black) means. Bottom panel: SpEx standard deviations of the 15 min (light blue), 30 min (dark blue), and 60 min (black) means. Meteorological periods shown as in Fig. 2.

Deleted: ¶

Formatted: Font: 10 pt

Deleted: 5

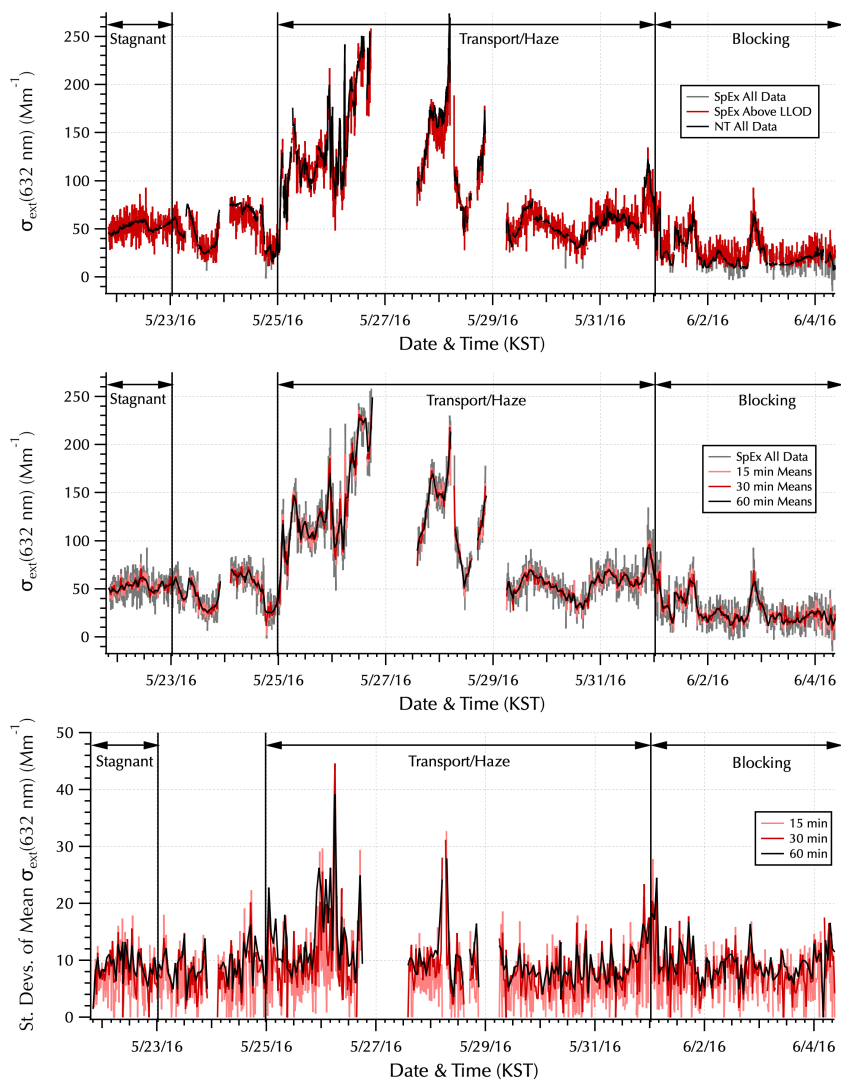


Figure S7. Time series of 632 nm σ_{ext} (Mm^{-1}) throughout the cruise. Top panel: SpEx (all data, gray; above LLOD, red; these curves are coincident except for when the lowest values are below detection and hence, appear gray) with NT σ_{ext} (black). Middle panel: SpEx (all data, gray) with 15 min (light red), 30 min (dark red), and 60 min (black) means. Bottom panel: SpEx standard deviations of the 15 min (light red), 30 min (dark red), and 60 min (black) means. Meteorological periods shown as in Fig. 2.

Formatted: Font: 10 pt

Deleted: 6

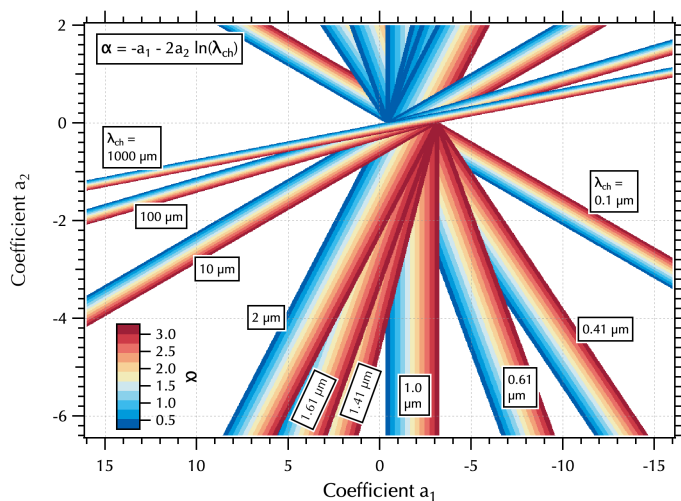


Figure S8. Illustration of the rotation of the mapping of α in (a_1, a_2) space as a function of λ_{ch} for long wavelengths. This illustration includes the extreme values of λ_{ch} of 100 and 1000 μm to stand in for the mapping that arises from using nm units instead of μm of wavelength.

Formatted: Font: Bold

Formatted: Font: Bold

Formatted: Font: Symbol

Formatted: Subscript

Formatted: Subscript

Formatted: Font: Symbol

Formatted: Subscript

Formatted: Font: 10 pt